

AD

AD-E402 790

Technical Report ARAED-TR-96013

STUDY OF CONSTITUTIVE MODELS FOR CONCRETE PENETRATION ANALYSIS

Vladimir M. Gold

December 1996



US ARMY
TANK AUTOMOTIVE AND
ARMAMENTS COMMAND
ARMAMENT RDE CENTER

U.S. ARMY ARMAMENT RESEARCH, DEVELOPMENT AND ENGINEERING CENTER

Armament Engineering Directorate

Picatinny Arsenal, New Jersey

Approved for public release; distribution is unlimited.

19970116 059

DTIC QUALITY INSPECTED 4

The views, opinions, and/or findings contained in this report are those of the authors(s) and should not be construed as an official Department of the Army position, policy, or decision, unless so designated by other documentation.

The citation in this report of the names of commercial firms or commercially available products or services does not constitute official endorsement by or approval of the U.S. Government.

Destroy this report when no longer needed by any method that will prevent disclosure of its contents or reconstruction of the document. Do not return to the originator.

REPORT DOCUMENT PAGE			Form Approved OMB No. 0704-0188	
Public reporting burden for this collection of information is estimated to average 1 hour per response, including the time for reviewing instruction, searching existing data sources, gathering and maintaining the data needed, and completing and reviewing the collection of information. Send comments regarding this burden estimate or any other aspect of this collection of information, including suggestions for reducing this burden, to Washington Headquarters Services, Directorate for Information Operations and Reports, 12115 Jefferson Davis Highway, Suite 1204, Arlington, VA 22202-4302, and to the Office of Management and Budget, Paperwork Reduction Project (0704-0188), Washington, DC 20503.				
1. AGENCY USE ONLY (Leave blank)	2. REPORT DATE December 1996	3. REPORT TYPE AND DATES COVERED Final		
4. TITLE AND SUBTITLE STUDY OF CONSTITUTIVE MODELS FOR CONCRETE PENETRATION ANALYSIS		5. FUNDING NUMBERS Target Defeat PE 622624 A ³ PE 622618		
6. AUTHORS(S) Vladimir M. Gold				
7. PERFORMING ORGANIZATION NAME(S) AND ADDRESS(ES) ARDEC, AED Energetics and Warheads Division (AMSTA-AR-AEE-W) Picatinny Arsenal, NJ 07806-5000		8. PERFORMING ORGANIZATION REPORT NUMBER		
9. SPONSORING/MONITORING AGENCY NAME(S) AND ADDRESS(ES) ARDEC, LSED Information Research Center (AMSTA-AR-LSL) Picatinny Arsenal, NJ 07806-5000		10. SPONSORING/MONITORING AGENCY REPORT NUMBER Technical Report ARAED-TR-96013		
11. SUPPLEMENTARY NOTES				
12a. DISTRIBUTION/AVAILABILITY STATEMENT Approved for public release; distribution is unlimited.		12b. DISTRIBUTION CODE		
13. ABSTRACT (Maximum 200 words) Three-dimensional axisymmetric calculation of penetration of concrete targets have been conducted with the CALE (Arbitrary Lagrangian Eulerian) code. All the constitutive models studied accounted for the compressibility of concrete and employed either solid or porous equation of state models; the influence of these models on the penetration calculations is studied and presented. This size of the plastic zone in front of the penetrator is estimated from the calculations for both compressibility models and is compared with the available experimental data. Comparison between the calculated values of the extent of this zone and the experimental data indicates that the porous equation of state model is more realistic in representing the elastic-plastic deformations in concrete. Effects of the initial porosity of concrete on penetration calculations are studied and discussed. The application of constant yield-strength and pressure-dependent yield-strength models for the concrete penetration analysis is studied, and the results of the calculations are presented and discussed. Crater profiles calculated with the pressure-dependent yield model showed good agreement with the available experimental penetration depths and the profiles of the tunnel portion of the crater.				
14. SUBJECT TERMS Concrete target Numerical analysis Penetration Plastic zone Projectile		15. NUMBER OF PAGES 43 16. PRICE CODE		
17. SECURITY CLASSIFICATION OF REPORT UNCLASSIFIED	18. SECURITY CLASSIFICATION OF THIS PAGE UNCLASSIFIED	19. SECURITY CLASSIFICATION OF ABSTRACT UNCLASSIFIED	20. LIMITATION OF ABSTRACT SAR	

CONTENTS

	Page
Introduction	1
Numerical Scheme and Material Models	2
Numerical Model	3
Results	5
Concrete Targets: The EOS Model	5
Concrete Targets: Yield Model	9
Conclusions	10
References	35
Distribution List	37

FIGURES

		Page
1	Schematic of target and crater resulting from projectile impact	13
2	Photograph of sectioned target	14
3	Initial configuration	15
4	Isolines of pressure at $35 \mu s$ for solid and porous ($\phi_0 = 0.18$) EOS models for concrete	16
5	Hole profiles calculated with solid and porous ($\phi_0 = 0.18$) EOS models for concrete	17
6	Profiles of axial component of velocity v_z vs axial coordinate z calculated for streamline $r = 0$ at time $t = 35 \mu s$	18
7	Profiles of radial component of velocity v_r vs radial coordinate r calculated at $z = 5.0 \text{ cm}$ at time $t = 35 \mu s$	19
8	Effect of EOD model for concrete on configuration of flow field in front of projectile - isolines of equivalent plastic strain	20
9	Effect of EOS model for concrete on configuration of flow field in front of projectile - profiles of equivalent plastic strain vs axial coordinate z for streamline $r = 0$	21
10	Effect of EOS model for concrete on configuration of flow field in front of projectile - isolines of σ_{zz} component of stress deviator	22
11	Trajectory of front end of penetrator compared with trigger times from break gages	23
12	Analysis with porous EOS model with values of initial porosity ϕ varying between 0.13 and 0.23	24
13	Isolines of porosity at time $t = 35 \mu s$ calculated with different values of initial porosity	25

FIGURES (cont)

		Page
14	Equivalent plastic strain vs radial coordinate r at $z = 5.0 \text{ cm}$ at time $t = 35 \text{ } \mu\text{s}$	27
15	Hole profiles calculated with constant strength model for varying values of von Mises strength Y	28
16	Hole profiles for constant strength models for concrete	30
17	Hole profiles for pressure-dependent strength models for concrete	30
18	Pressure-dependent yield surface $Y = Y(p)$	31
19	Trajectory of front end of projectile	32

TABLES

1	Computations performance for $200 \text{ } \mu\text{s}$ of penetration time	33
2	Parameters for solid and porous EOS constitutive models	33

SYMBOLS AND ABBREVIATIONS

<u>Notation</u>	<u>Definition</u>
E	internal energy
p, p_c	pressure, compaction pressure
r	radial coordinate
u	penetration rate
v	velocity of the rigid portion of the penetrator
v_r and v_z	radial and axial component of the velocity
Y	von Mises yield stress
z	axial coordinate
$\varepsilon_{1p}, \varepsilon_{2p},$ and ε_{3p}	principle plastic strain components
Δ_p	size of the plastic zone in front of the penetrator
$\rho, \rho_0,$ and ρ_r	density, initial density, and reference density, respectively
ρ_p and ρ_t	density of the penetrator and the target, respectively
σ_n	normal stress at a boundary
φ, φ_0	porosity, initial porosity

INTRODUCTION

When a high-velocity projectile impacts a target, the penetration is accomplished by displacing the target material radially, and as a result, a tunnel shaped crater is formed in the target. The depth and the diameter of the produced hole depend upon the projectile velocity and the material properties of the projectile and the target. In particular, the "flow" of the target material under the pressure exerted by the projectile is very sensitive to the nature and mode of failure of the target material. Concrete is a very complex material, consisting of mineral aggregate bound by cement paste containing a large amount of water and voids. As a result, it is only recently that the behavior of this complex material in response to high-velocity penetration has begun to be understood.

Only a limited number of three-dimensional concrete penetration calculations have been reported in the literature. These calculations (refs 1 to 3) pertain to simulations of low velocity impacts and employ codes based on a Lagrangian formulation of the governing equations. Since in case of low velocity impacts, the projectile is subjected to relatively small deformations and remains relatively rigid and nondeformed, the Lagrangian approach can offer some computational advantages. However, even when the deformations of the penetrator are relatively small, the target elements adjacent to the penetrator front are deformed severely and cannot "flow" around the penetrator. To overcome this difficulty requires frequent re-zoning of the target material in the neighborhood of the penetrator front. The re-zoning adds to the computation time and allows for variability in the results, depending on the type of the re-zoning algorithm and the frequency of re-zoning (ref 1). A number of issues and techniques applicable to the penetration calculations with Lagrangian codes are discussed in reference 1.

The concrete constitutive models employed in all the above mentioned studies exhibit limited features such as pressure-dependent yield surfaces (refs 1 and 2), pressure and strain-rate-dependent yield surfaces, and pressure-dependent bulk and shear moduli (ref 3). Hydrocode implementation of the existing advanced concrete models encounter a number of computer code development challenges. This is mainly due to the extensive computational resources required for the calculations. Recently, a number of advanced models that are capable of adequately modeling the complex dynamic behavior of concrete has been reported in the literature. Among these models are the Bicanic and Zienkiewicz model (refs 4 and 5) and the porous material models (refs 6 and 7).

In this work, state-of-the-art advanced models for concrete are applied to a problem of high-velocity penetration, enabling the prediction of the target cratering and hole shape. A schematic of a crater produced in a concrete target (ref 8) is shown in figure 1. The entrance portion of the crater is produced by the spallation of concrete in the vicinity of the impact site. The crater entrance is typically wide and shallow, rapidly evolving into a well rounded and slightly tapered tunnel. The penetration prediction capability of various constitutive models for concrete, which were studied in this work, was assessed using the shape of the latter portion of the crater only. The accuracy of the penetration prediction

capability of these models was established by comparing the numerical results to experimental data (ref 8).

When the rate of penetration in concrete is below the sonic velocity, a zone of comminuted concrete is formed in front of the penetrator, and the extent of this zone is influenced by the dynamic properties of the target material. A number of experimental techniques for acquisition of the subsonic target material flow in front of the penetrator are reported in the literature (refs 9 and 10). Unique data of the dynamic behavior of concrete have been obtained and reported earlier (ref 8) using a sequence of break gages. These data, as well as, numerous experimental and analytical studies of penetration with high length over diameter (L/D) ratio projectiles indicate that the trajectory of the front end of the penetrator consists of two distinct regions: a long region of approximately steady state penetration and a short region of deceleration. A photograph of a sectioned target from these experiments is shown in figure 2. Break gages that were originally plain are uniformly bulged out in the direction of the projectile motion. Note that all gages are approximately parallel to each other, which may lead to a conjecture regarding the steady-state motion of the penetrator in the target.

The technique for determining the extent of the plastic zone in front of the projectile is based on the fact that the projectile penetration rate in the steady-state region depends strongly on the densities of the projectile and the target, and only weakly on their strengths. This allows an accurate prediction of this region of the trajectory without detailed knowledge of the constitutive behavior of the target material. In the experiments by Gold et. al. (ref 8), break gages were placed along the projectile trajectory in a region of steady-state penetration. Voltages applied to the gages were monitored for sudden interruptions (i.e., for "breaks" of the gages), which were associated with the time of arrival of the front of the zone of fractured concrete. Once the trajectory of the projectile front end is calculated, the extent to the zone of comminuted concrete can be measured as the difference between the trajectory and the regression of trigger times of the break gages.

In the present work, the numerical simulations have concentrated on modeling an earlier experiment involving a 19-cm long and 1.3-cm dia copper projectile impacting a plain concrete target with velocity $V_0 = 0.1836 \text{ cm}/\mu\text{s}$ (ref 8). The projectile was carefully aimed along the target axis, and x-ray records confirmed a 90-deg incident angle at the impact. These experimental conditions simulated an axially symmetrical configuration, and the analytical study was reduced to a three-dimensional axially symmetrical problem. This work presents results of numerical calculations using various constitutive models for concrete.

NUMERICAL SCHEME AND MATERIAL MODELS

The numerical simulations presented in this work were performed using the CALE (ref 11) computer program. The CALE is the plane two-dimensional and three-dimensional

axisymmetric hydrodynamics code based on an Arbitrary Lagrangian Eulerian (ALE) formulation of the governing equations. It is capable of modeling multi-material flows and allows for discontinuous velocities at material interfaces. In addition to the specification of the problem geometry and initial and boundary conditions, the equations of state (EOS) and the constitutive equations for the target and the projectile have to be specified before the solution procedure can be initiated.

The constitutive equation for the projectile material adopted here is that of Steinberg-Guinan (ref 12), which specifies the shear modulus and the yield-strength as a function of pressure, temperature, and equivalent plastic strain. The EOS that was used to model the hydrodynamic response of copper was the standard linear polynomial approximation usually employed for metals (ref 11). Since the copper projectiles were manufactured from a standard stock of oxygen-free high conductivity copper (OFHC), the analysis relied on a standard set of parameters for this material from reference 13. Details of these models and their implementation can be found in reference 11.

Two constitutive models were used to represent the behavior of concrete:

- An elastic-plastic model with von Mises yield surface
- An elastic-plastic model with pressure-dependent yield surface

The sensitivity of the impact response of concrete to the selection of an EOS, a constitutive model, and relevant parameters was studied in this work. Details regarding these models and results of the calculations are discussed later.

NUMERICAL MODEL

The geometry and boundary conditions are shown in figure 3. The domain considered is axisymmetric in r - z space. Domain $T_1T_2T_3T_4$ represents the target, $P_1P_2P_3T_1$ is the spherical-nose projectile, and the rest of the domain $E_1E_2T_2T_1$ is filled with air. Eight 0.03-cm thick break gages were initially modeled using three computations cells, each 0.01-cm thick, filled with copper. After some initial numerical experimentation it became clear that these 0.01-cm cells were resulting in very small time steps, which controlled the overall speed of calculations. Therefore, in order to decrease the otherwise prohibitively excessive computational time, the number of cells across the thickness of the break gages was reduced to one.

The following boundary conditions were applied along the boundary of domain $E_1E_2T_3T_4$:

$$v_r = v_z = 0 \quad \text{along } E_1E_2$$

$$\sigma_n = 0 \quad \text{along } E_2T_3 \text{ and } T_3T_4$$

$$v_r = 0 \quad \text{along } E_1T_4 \text{ (line of axial symmetry)}$$

The portion of the mesh $A_1A_2T_3T_4$ was run in ALE mode, but the nodes within the domain $E_1E_2A_2A_1$ were reset to their original position after each cycle of calculations. Attempts to run the domain $E_1E_2A_2A_1$ in ALE mode resulted in severe deformations and tangling up of the ALE mesh due to the debris of concrete ejected from the crater and moving away from the target surface. This significantly reduced the time step, slowed down calculations, and often caused termination of the run. The present work primarily concentrated on simulating the formation of the crater, rather than on a study of a spallation off the front surface of the target, which would require a detailed analysis of the motion of this debris. Therefore, spacing the nodes in domain $E_1E_2A_2A_1$ coarsely and "running" them in the Eulerian mode significantly sped up the calculations. Thus, a significant increase in the computational speed was achieved, although, at an acceptable loss of accuracy of the analysis in that region. In a few trial runs, the portion of the grid contained in $R_1E_2A_2R_2$ was omitted, the free boundary was set along R_2A_2 and the boundary conditions $v_r = v_z = 0$ were imposed along R_1R_2 . This allowed a slight reduction in the number of computational zones and sped up the calculations. However, it was determined that the grid motion algorithms were very sensitive to variations in the values of the parameters appearing in the material models, which would in turn complicate the course of the parametric studies. Thus, this approach was abandoned.

A non-uniform distribution of nodes in both the radial and axial directions was employed in the discretization model. The computational mesh for all the zones was designed based on the rationale that the best accuracy of analysis would be achieved with fine degrees of discretization in the areas subjected to high gradients, and a coarser mesh in regions with moderate gradients. The finest radial grid size Δr_{\min} was set along the path of motion of the projectile where the material deformations are the most severe. The radial grid size gradually increased toward the maximum Δr_{\max} at the lateral boundary. In the axial direction, zones 1 through 4 (fig. 3) denote regions with different axial grid sizes Δz . Nodes in zone 2 were spaced uniformly. In zones 1, 3, and 4 axial grid sizes increased gradually from the smallest Δz_{\min} at one boundary to the largest Δz_{\max} at the opposite boundary. The axial size of zone 3 was selected according to the expected depth of penetration. In zone 4, which is beyond the expected depth of penetration, nodes were spaced coarsely (in the axial direction). In order to resolve the formation of the crater entrance, the grid in zone 1 was finely meshed close to the target surface, while the size of the computational mesh gradually increased toward the boundary E_1E_2 .

The effect of the grid size on the overall accuracy of the calculations is summarized in table 1. In all cases the computational mesh had a similar configuration, but the total number of the computational elements varied for 29,895 to 9,437. Reduction of the total number of elements from 29,895 to 10,971 was achieved by increasing the zone of the elements in zones 2 and 3 by a factor of two, which cut the required CPU time of SUN

4/490 for a sample 200 μ s long event from 102.2 to 18.4 hrs. Reduction of the number of elements from 10,971 to 9,437 was achieved by changing the number of cells across the thickness of the gages from three to one, which increased the computational speed by a factor of about two. Since this study concentrated on the concrete, this approach had no appreciable effect on the accuracy of the calculations. Changes in the modes for controlling grid motion from mixed Euler/ALE to purely Eulerian analysis significantly affected the speed of calculation reducing it (for the Eulerian analysis) by a factor of about three. Calculated crater profiles compared at 200 μ s were nearly the same for all cases with only slight differences in the resolution of the crater lip formed by the ejected debris of concrete. Since the accuracy of analysis was not affected either by varying the number of computational cells or by changing modes of grid motions, the mesh configuration resulting in the lowest CPU time (pci0_02) was adopted for all parametric studies presented in this work.

RESULTS

Concrete Targets: The EOS Model

An estimate for the low bound of pressures exerted on the concrete at the front end of the projectile impacting with velocity $v_0 = 0.1836 \text{ cm}/\mu\text{s}$ can be obtained from the ideal one-dimensional hydrodynamic theory of penetration (ref 13). Indeed, the following equation:

$$p = \frac{1}{2} \rho_p (v - u)^2 = \frac{1}{2} \rho_t u^2 \quad (1)$$

with $\rho_p = 8.9 \text{ g}/\text{cm}^3$ for copper projectile and $\rho_t = 2.24 \text{ g}/\text{cm}^3$ for concrete, yields $u = 0.122 \text{ cm}/\mu\text{s}$, which gives a value for the pressure of $p = 16.7 \text{ Kbar}$. More realistic estimates of the pressure are obtained from three-dimensional axisymmetrical elastic-plastic analysis which yields values of the order of 20 to 27 Kbar (fig. 4). At these high pressures, which exceed the static unconfined strength of concrete by almost two orders of magnitude, the effects of compressibility of the target material are of significant importance.

Experimental shock-wave studies for concrete conducted by Gregson (ref 14) reveal significant non-linearity in Hugoniot data for particle velocities below 0.1 cm/ μ s. Non-linearity in the Hugoniot can be attributed to physical mechanisms of micro-cracking and pore closing. Read and Maiden (ref 15), using a porous EOS model, were able to reproduce the essential features of the experimental shock velocity vs particle (material) velocity data. The particle velocities experienced by the concrete in the earlier penetration experiments (ref 8) are in the very same range. Therefore, applying the porous EOS model is appropriate for describing the constitutive response of concrete.

Following Tipton (ref 6), the porous EOS model assumes that, while in compression, the porosity is not changed until the pressure exceeds the compaction pressure, p_c . In tension, the porosity is not increased until the pressure drops below $-p_c$. The compaction pressure is assumed to be a function of the porosity ϕ and has the following form:

$$p_c = p_o \log(\phi) \quad (2)$$

The total pressure of the porous material is given by

$$p = (1 - \phi)p_s(\rho_s) \quad (3)$$

where ϕ is the porosity, and p_s and ρ_s are the pressure and the density of the solid phase, respectively. The EOS for the solid phase is taken in a polynomial form:

$$p = A_o + A_1\mu + A_2\mu^2 + A_3\mu^3 + (B_o + B_1\mu + B_2\mu^2)E \quad (4)$$

where $\mu = \rho / \rho_r - 1$, $\rho_r = \rho_o / (1 - \phi_o)$ is reference density, and ϕ_o is the initial porosity. Further details on this model and its implementation in CALE can be found in reference 11.

A comparison of various flow field variables calculated with solid (i.e., directly via equation 4 and porous (i.e., using equations 3 and 4) EOS models are presented in figures 4 to 11. The values of parameters for these constitutive models are given in table 2. The coefficients appearing in the polynomial EOS form were adopted from reference 11 and are based upon the Hugoniot data from reference 14. In all cases, the calculations were carried out up to $800\mu s$. All calculations show that the projectile almost completely erodes at 300 to $400\mu s$, and the penetration process essentially ceases at approximately $500\mu s$. Figure 5 compares the experimental data with the calculated final hole profiles at $500\mu s$. Regardless of the EOS model (as well as other models to be considered later), the entrance portion of the crater is predicted poorly. All numerical calculations presented in this work failed to reproduce not only the size of the entrance, but mostly importantly, even the general shape of this portion of the crater. Since the entrance portion of the crater is produced by spallation of concrete in the vicinity of the impact site, its size and shape are strongly influenced by brittle fracture, a phenomenon that was not modeled in the present work. Experiments show that the crater entrance is typically wide and shallow, rapidly evolving into a well rounded and slightly tapered tunnel. The penetration prediction capability of various constitutive modes for concrete studied, was assessed using the shape of the latter portion of the crater only. The accuracy of the penetration prediction capability of these models was established by comparing the numerical results to experimental data (ref 8). Both calculations (fig. 5) significantly disagree with the experimental data. Formation of the tunnel portion of the crater is accomplished through plastic flow of the target material, driven by the pressure exerted at the interface between the projectile and the target. Under these conditions, this material is always under

compression and is far removed from the region of the crater entrance where the material is in tension and is subjected to brittle fracture. Therefore the influence of the brittle properties of concrete on the formation of the tunnel portion of the crater is negligible. Experimental data indicate that the shape of this portion of the crater is similar to the shape of boreholes in ductile materials, such as metals, etc. (ref 8).

Comparisons of results obtained with the solid and porous EOS models reveal that the hole profile computed with the porous model is slightly deeper and almost twice as wide as the profile predicted with the solid model. From the point of view of a one-dimensional modified hydrodynamic theory of penetration, the penetration depth is a function of the pressure at the front end of the projectile. Thus, the average pressures computed with the porous EOS model were slightly lower than with the solid EOS model, and this is in agreement with the Hugoniot data from shock-wave studies.

Figure 4 presents plots of isolines of pressures computed at approximately $35\mu s$. Although most of the penetration process is quasi-steady state, the calculated pressures reflect specific wave propagation patterns which are very sensitive to material models. Both plots shown in figure 4 are taken at approximately the same time; however, the computed wave propagation patterns reflect slightly different wave propagation states. This explains the fact that the maximum pressure recorded in the plot for the porous EOS model is higher than that for the solid EOS model. Nevertheless, for the solid EOS model, the overall pattern of widely spread isolines of pressure is distinctly different from pressure distributions computed with the porous EOS model. This essentially confirms the qualitative features that are expected from "snow plow" type of EOS model.

The calculated velocity fields are less prone to fluctuations (due to stress wave propagation) and are quasi-steady state. Figure 6 shows profiles of the axial component of velocity along the centerline at time $35\mu s$. The interface between projectile and concrete is located approximately at $z^* = 4.4\text{ cm}$, and although in the projectile ($z < z^*$) the velocity profile is the same, the distribution of the velocities in the concrete ($z > z^*$) is quite different. The velocity profile calculated with the solid EOS model is smooth and the flow spreads out for significant distances in front of the projectile. The situation is quite opposite for the porous EOS model. The flow is contained in the immediate vicinity of the penetrator front and is rapidly diminished away from it. The same fact is established from comparison of the radial flow fields shown in figures 6 and 7. As with the axial velocity profiles, for the solid EOS model, the profile of the radial component of velocity is smooth and spread out, while for the porous EOS, the flow field is more intense and confined. Since final hole diameters are proportional to the magnitude of the radial flow, the porous EOS model is expected to result in significantly wider holes, which in turn, correlates with the results presented in figure 5.

Results presented in figures 8 to 10 summarize the effects of the EOS model on the flow field structure in front of the projectile. Calculated patterns of isolines of the equivalent

plastic strain are shown in figure 8. The equivalent plastic strain is defined as:

$$\gamma = \frac{2}{3} \sqrt{(\varepsilon_{1p} - \varepsilon_{2p})^2 + (\varepsilon_{2p} - \varepsilon_{3p})^2 + (\varepsilon_{3p} - \varepsilon_{1p})^2} \quad (5)$$

where ε_{1p} , ε_{2p} , and ε_{3p} are the principal plastic strain components, and reflects the extent of elastic-plastic state. Isolines of a small γ mark the position of the elastic-plastic boundary in concrete. A Comparison between these two plots yields that the sizes of plastic zones in front of the projectile are remarkably different for the two EOS models. A plot of equivalent plastic strain along the streamline $r = 0$ is shown in figure 9. Consistent with the previous results for the porous EOS model, the plastic flow is more intense and confined to a short zone in front of the projectile. The position of the elastic-plastic boundary is distinct and the approximate size of the plastic zone in concrete in front of the projectile can be measured directly from the plot, yielding $\Delta_p \approx 1.3 \text{ cm}$. The size of the plastic zone can also be verified from the plot of isolines of the σ_{zz} component of stress deviator shown in figure 10.

In figure 11 the calculated trajectory of the front end of the projectile is compared with the recorded sequence of trigger times from the break gages in the study in reference 8. The EOS model for concrete employed is shown to have no effect on the calculated trajectory, which is almost identical for both models. The trigger times from the gages refer to significant deformations exerted on the copper foils that are sufficient to break them causing interruption in the applied voltage. This event is approximately coincident with the time of arrival of the elastic-plastic boundary. The distance between the regression of trigger times and the trajectory measures the size of plastic zone in front of the projectile, which according to figure 11, yields approximately $\Delta_p \approx 1.3 \text{ cm}$. As seen from figure 9, this measurement of the plastic zone, correlates well only with results obtained using the porous EOS model. A very poor agreement in the size of the plastic zone is obtained in case of the analysis using the solid EOS model. Hence, in spite of relatively "better" predictions of crater size with the solid EOS model (both calculations significantly disagree with the experimental data (fig. 5), this fact provides experimental evidence that the porous EOS model is more realistic in describing the effects of elastic-plastic flow in concrete.

The initial porosity ϕ_0 is one of the parameters appearing in the porous EOS model, and the sensitivity of penetration calculation to the values of ϕ_0 are presented in figures 12 to 14. The measured value of initial porosity of Gregson's (ref 14) concrete was $\phi_0 = 0.18$, and this value was adopted as a baseline in this work. Figure 12 exhibits hole profiles at $500\mu\text{s}$ calculated with values of initial porosity of $\phi_0 = 0.13$, $\phi_0 = 0.18$, and $\phi_0 = 0.23$, and the same initial density $\rho_0 = 2.24\text{g/cm}^3$. The values of other parameters for the concrete material model are given in table 2. Computational experiments indicated that varying the value of initial porosity from 0.13 to 0.23 resulted in nearly identical penetration depths and hole profiles. Figure 13 presents plots of isolines of porosity calculated for varying values of ϕ_0 , which suggest a cause for the weak correlation between the calculated hole profiles and the initial porosity. As projectiles penetrate the target, concrete adjacent to the

boundary of the forming crater is crushed and all porosity is squeezed out. Since in all cases the crushed concrete was brought to the same state with $\phi_o \rightarrow 0$, the further motion of this material is nearly identical, which results in similar hole profiles. Physical models for concrete can be approximated by a composite material composed of a crushable cement matrix and an aggregate. Varying the value of initial porosity while keeping the initial density constant, implies materials with the same average density and varying size of the aggregate. From the point of view of the one-dimensional hydrodynamic theory of penetration, the penetration depth is a function of the target material density and since the initial density was the same, this correlates with the calculations presented in figure 12.

In comparing solid and porous ($\phi_o = 0.18$) EOS models, distinct features are observed in calculated flow variables that are characteristic to each of these models. For the numerical validity and consistency of the models, it would be reasonable to expect that, with decreases in the initial porosity, the characteristic flow variables would asymptotically approach variables calculated with the solid EOS. As representative of variables characteristic for the flow, radial profiles of equivalent plastic strain were selected, and are shown in figure 14. Comparison of these plots reveals a definite tendency for gradual increases of the size of the plastic flow field with decreases in the initial porosity, which transition to the asymptotic level calculated with the solid EOS.

Concrete Targets: Yield Model

Another aspect of the present work is the selection of a material model for concrete and a set of parameters which reproduce the experimentally observed penetration depth and the profile of the tunnel portion of the crater. These two penetration characteristics are governed primarily by a constitutive model which describes the elastic-plastic behavior of the target material under compression exerted by the projectile. The first model studied was a simple model of an ideal elastic-perfectly-plastic behavior with constant yield strength. This model has only one adjustable parameter, (von Mises strength Y) which can be varied to match the experimental data. However, it is not physically realistic for the description of the complex behavior of geologic materials.

Figure 15 shows hole profiles calculated with a constant yield-strength model with varying values of von Mises strength Y . The unconfined compressive strength of the concrete used in the experiments (ref 8) was 0.374 Kbar, and in the numerical experiments, the value of von Mises yield-strength was varied from $Y = 0.187$ Kbar to $Y = 1.8$ Kbar. The results represented in figure 15 indicate that the calculated hole profiles were insensitive to the value of von Mises yield in the constant yield model.

The validity of the concrete models employed in the numerical analysis presented in this work is established through comparison with the following experimental data:

- The size of the elastic-plastic zone in front of the projectile

- Hugoniot data from the shock wave studies of Gregson (ref 14)
- The resulting profile of the tunnel portion of the crater

In contrast to the earlier results that employed a constant strength yield model, figures 16 and 17 present the results of calculations based on a model with a pressure dependent-yield surface. The analysis presented in the earlier section showed that the solid EOS model failed to reproduce the experimentally observed size of the plastic zone in front of the projectile. This result is in agreement with the shock wave studies (ref 14), which show that the Hugoniot data for concrete cannot be reproduced adequately by a solid EOS model. Both results demonstrate that when the physical mechanism of concrete failure due to pore closure is included into the EOS model, only then the structure of the plastic flow is modeled accurately. Thus, further numerical experimentation with a solid EOS model was abandoned. All further calculations employing either the constant yield-strength model or the pressure dependent yield model were performed using the porous EOS model only. Comparison of the size of the plastic zone in front of the projectile calculated in all these numerical experiments (table 2) indicated that varying the value of the von Mises yield-strength in the constant-strength model did not affect the size of this zone. However, using the pressure-dependent yield-strength model, not only was the experimental depth of penetration reproduced, but also the measurements of the profile of the tunnel portion of the crater were matched.

The configuration of the yield surface $Y = Y(p)$ that was used in these calculations was adopted from Smith (ref 16) (figs. 18 and 19). Figure 19 compares the calculated penetration histories of $Y = \text{const}$ and $Y = Y(p)$ models. According to the one-dimensional hydrodynamic theory of penetration, the penetration into the target is achieved through the erosion of projectile material. With the higher rates of erosion of projectile material, lower depths of penetration are expected. The velocities of the front end of the projectile are noticeably different for the two models, and the rate of projectile erosion for $Y = Y(p)$ model is greater than for $Y = \text{const}$ model (fig. 19).

CONCLUSIONS

The structure of the flow field around the penetrator is the most important element that governs a number of penetration parameters including the target resistance to penetration, and the depth and the diameter of the produced hole. Since concrete is a very complex material, a number of models have been developed to describe its response to high rate and high strain deformations. Since the choice of the constitutive model affects the elastic-plastic zone surrounding the penetrator, several candidate models were studied using three-dimensional axisymmetric analysis. The calculated size of the elastic-plastic zone was found to be extremely sensitive to the choice of the model. Therefore, the physical validity of the various concrete models was established from comparison between the analysis and the existing experimental measurements of the size of the comminuted

concrete zone. From all the models tested, only the porous equation of state model resulted in the elastic-plastic zone size predicted by the experimental dynamic measurements. This substantiated the theoretical claims that the porous equation of state is currently the most realistic model for representing the elastic-plastic flow in the concrete medium. A number of yield-strength models were examined for modeling the constitutive behavior of concrete. However, the pressure-dependent yield model is the only one that resulted in hole profiles which agreed with experiments. Finally, the present work established a reliable material model for concrete targets for the prediction of concrete penetration for a wide range of ballistic impact velocities.

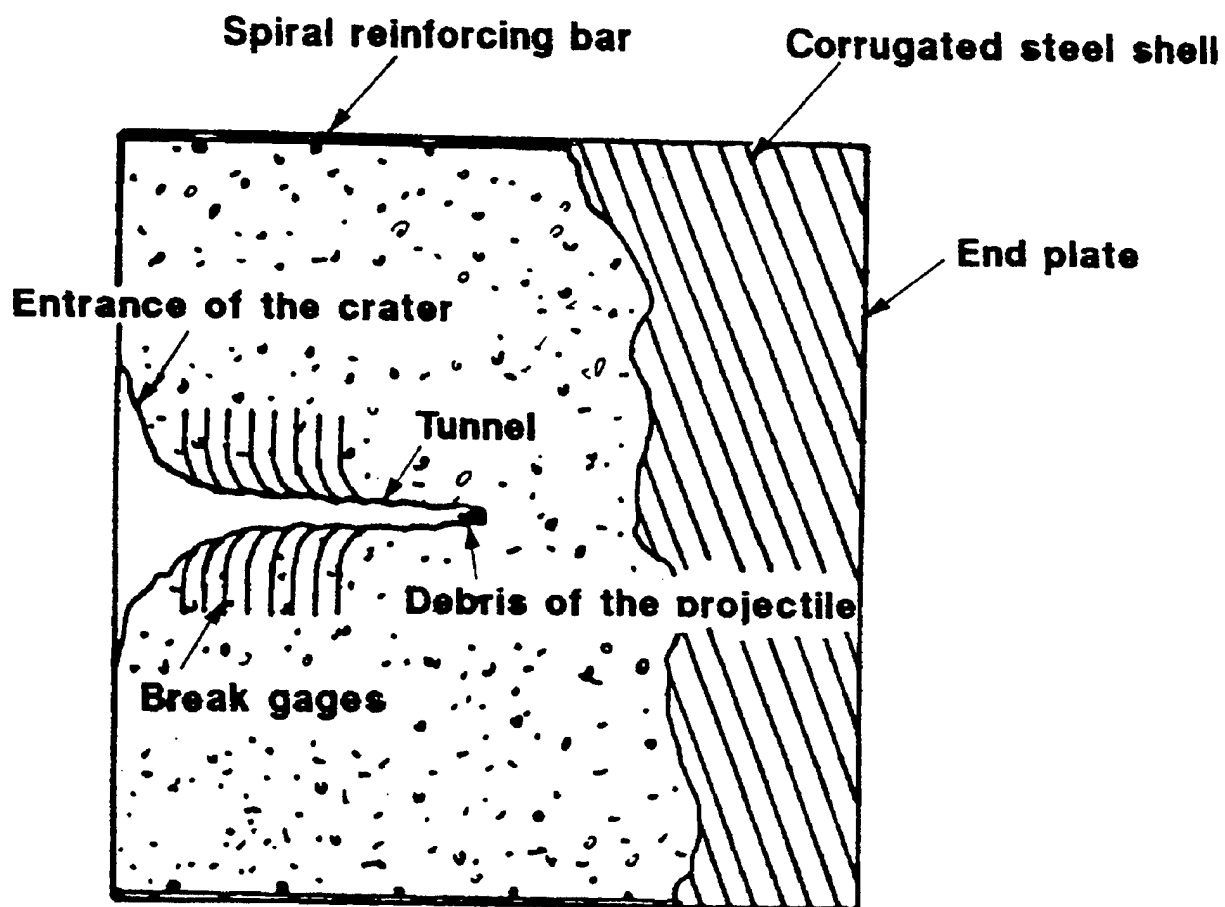


Figure 1
Schematic of target and crater resulting from projectile impact

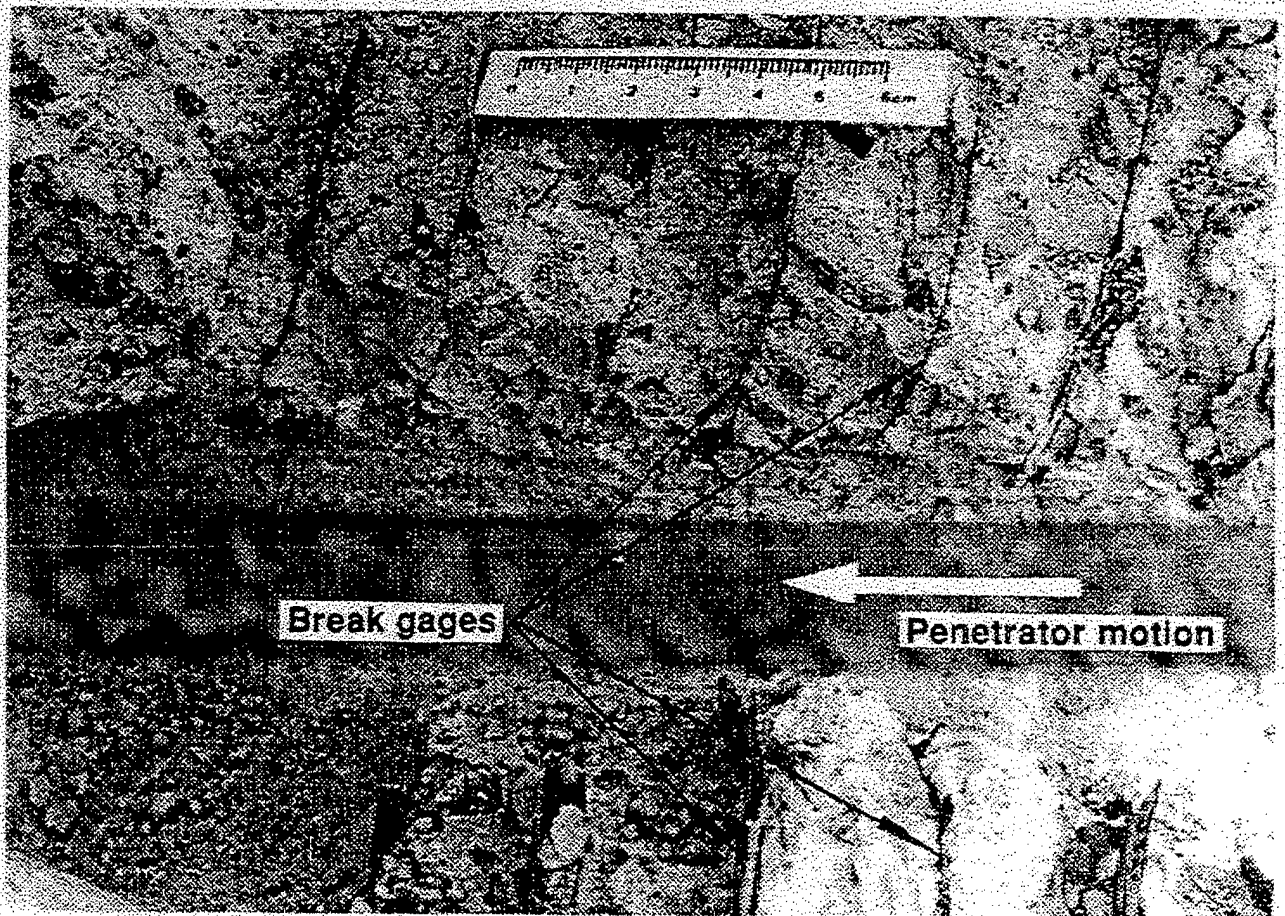
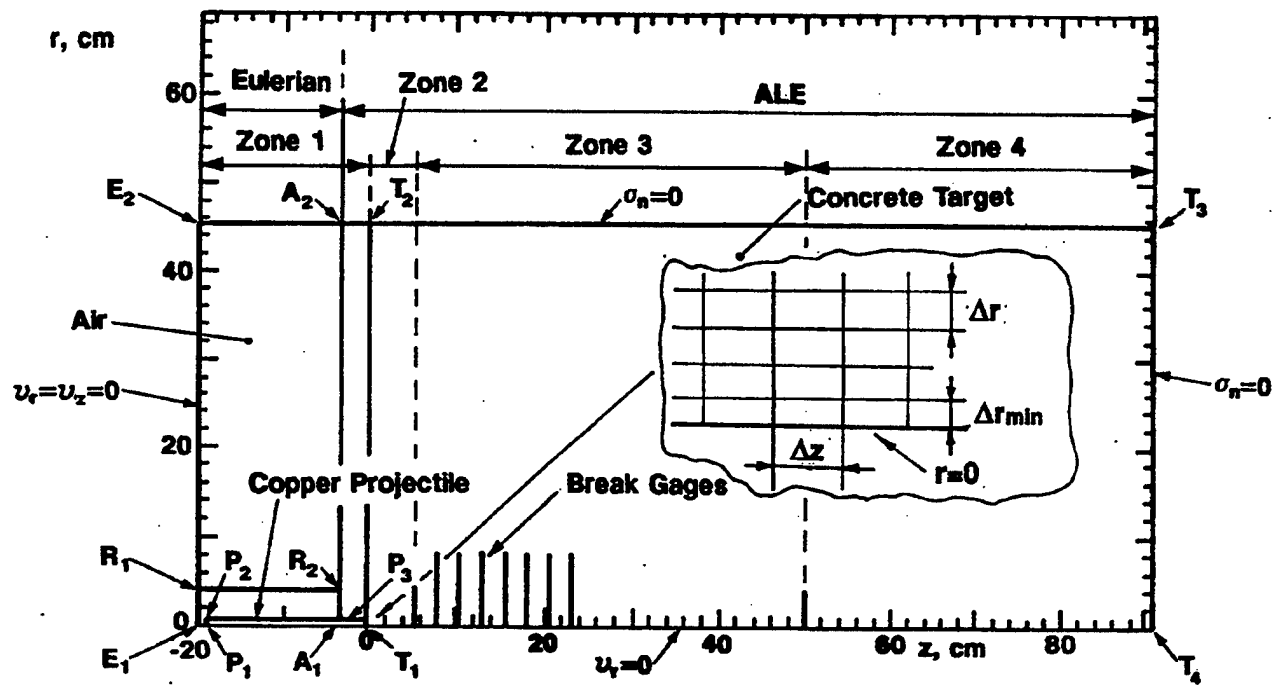


Figure 2
Photograph of a sectioned target



(Spherical-nose copper projectile impacting
right circular cylinder of concrete with velocity
 $V_0 = 0.1836 \text{ cm}/\mu\text{s}$.)

Figure 3
Initial configuration

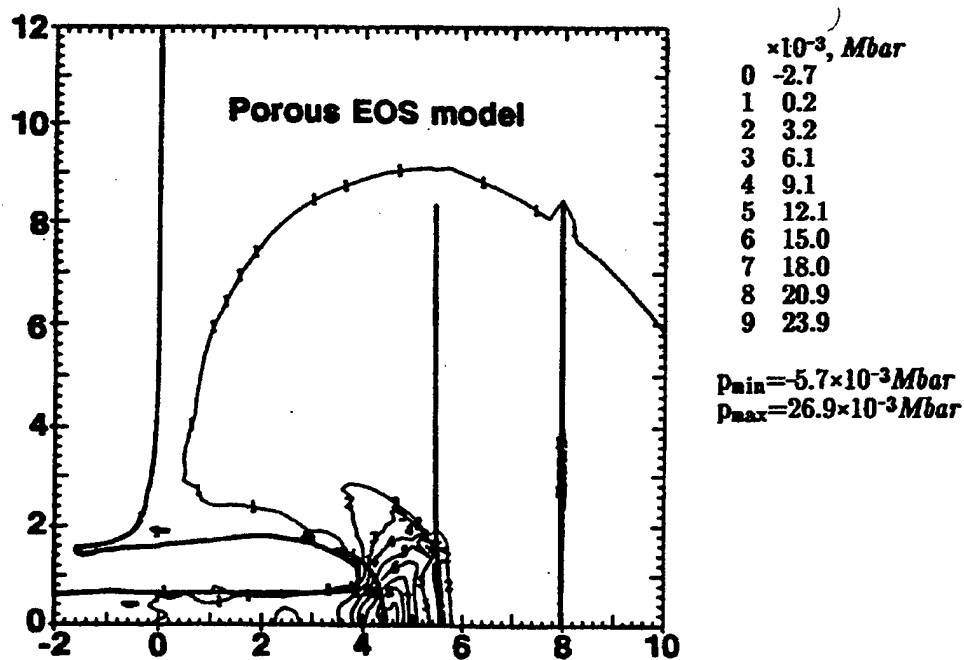
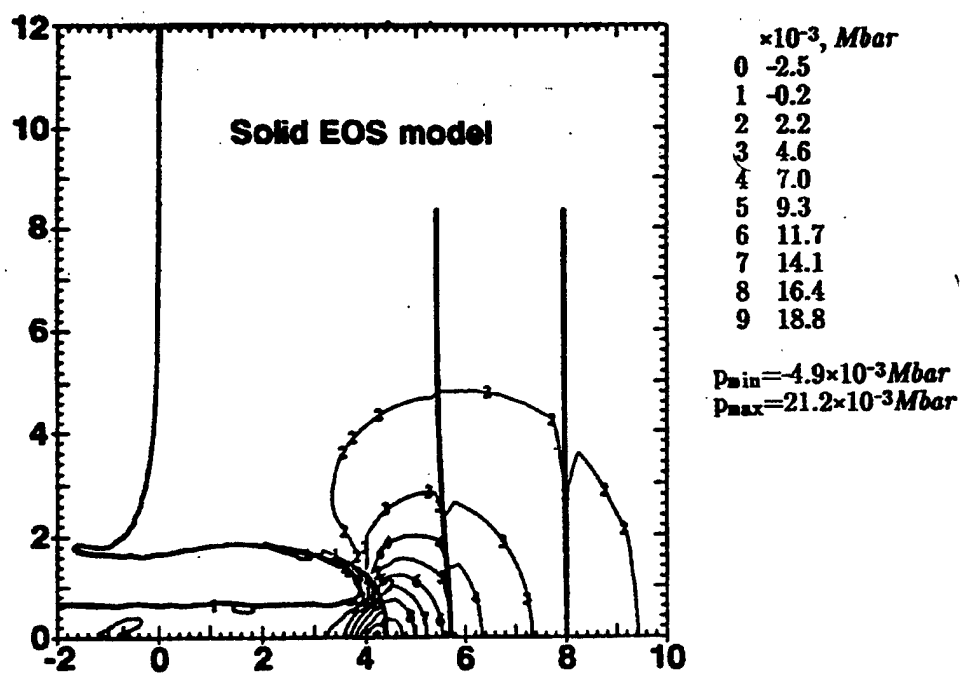


Figure 4
 Isolines of pressure at $35 \mu\text{s}$ for solid and porous
 ($\phi_0 = 0.18$) EOS models for concrete

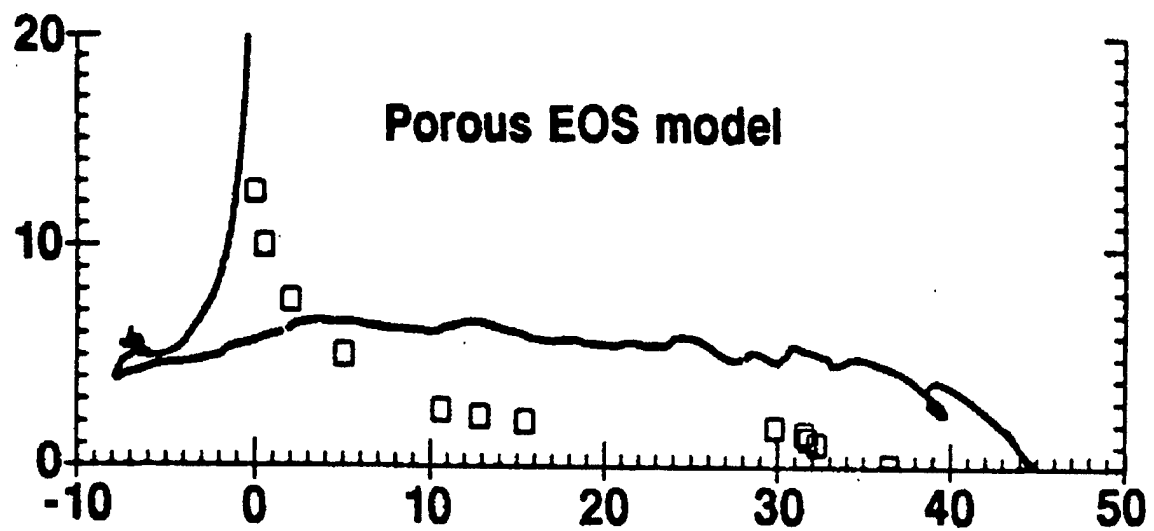
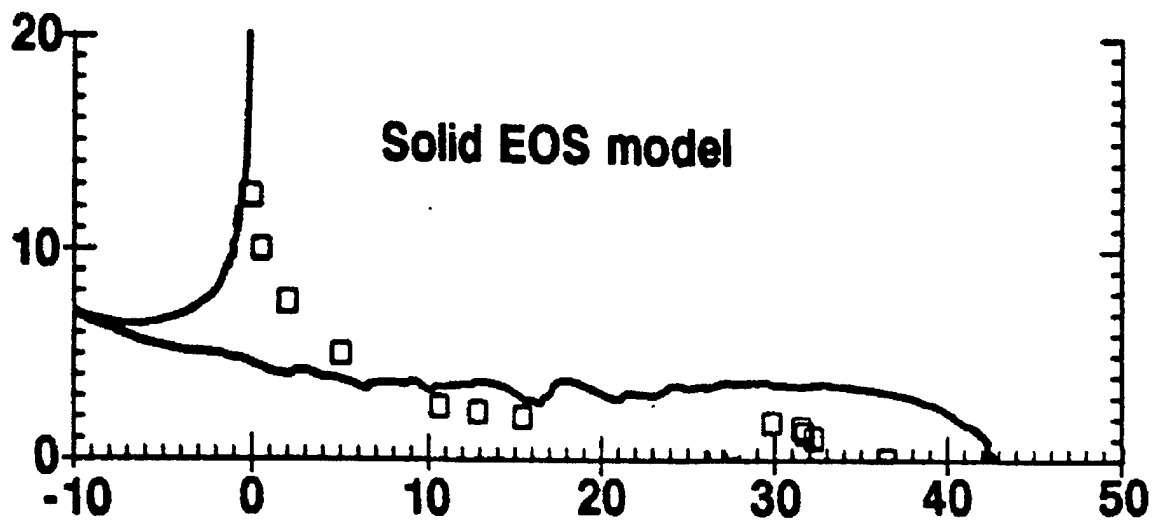


Figure 5
Hole profiles calculated with solid and porous
($\phi_0 = 0.18$) EOS models for concrete

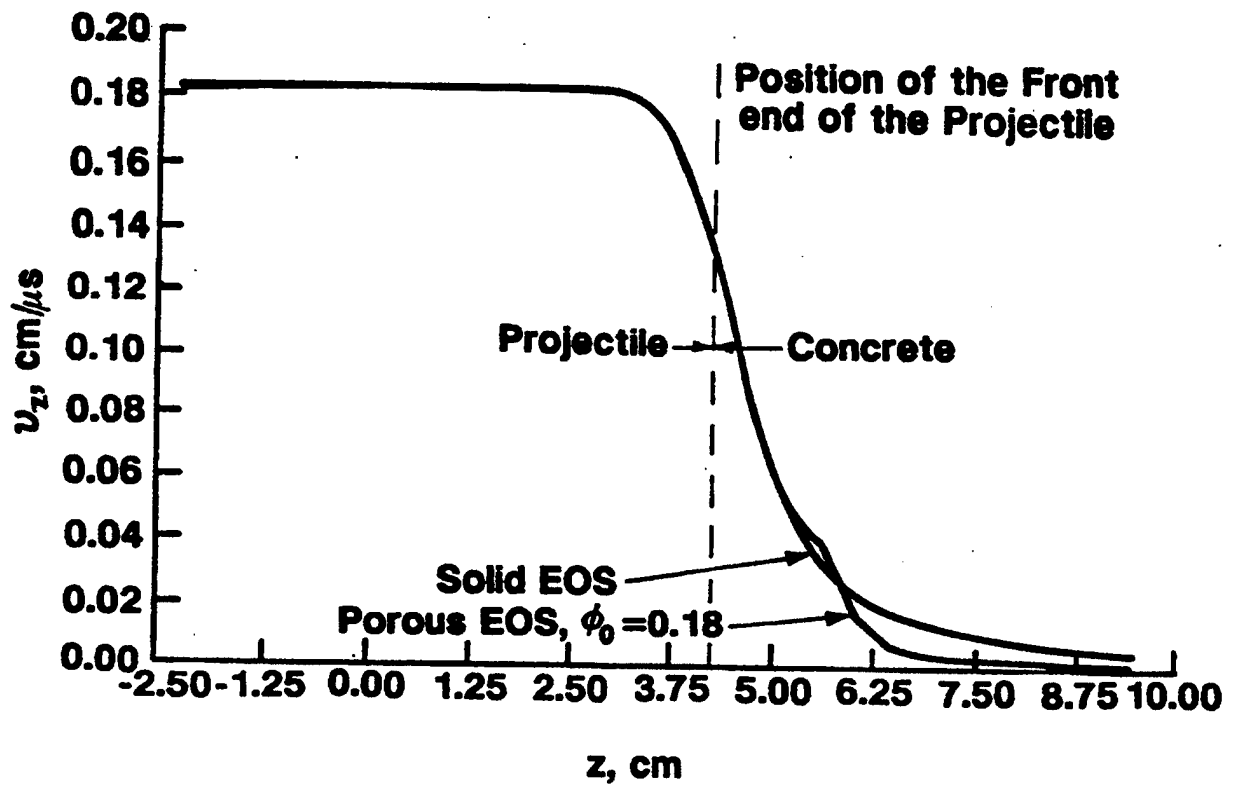


Figure 6
Profiles of axial component of velocity v_z vs axial coordinate z calculated for streamline $r = 0$ at time $t = 35 \mu s$

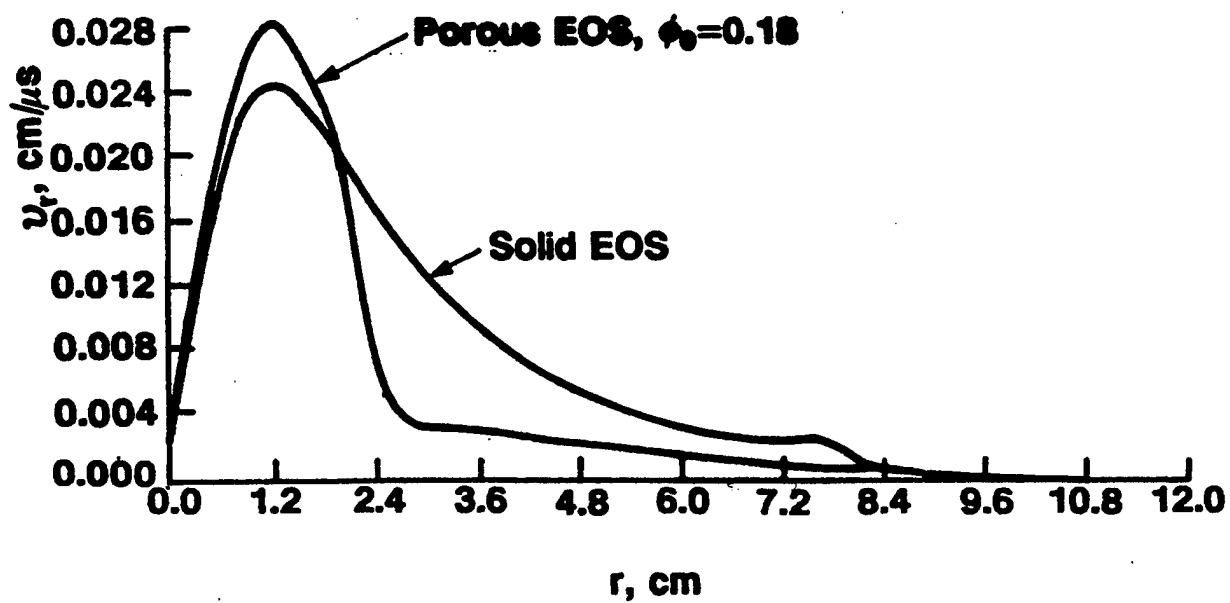
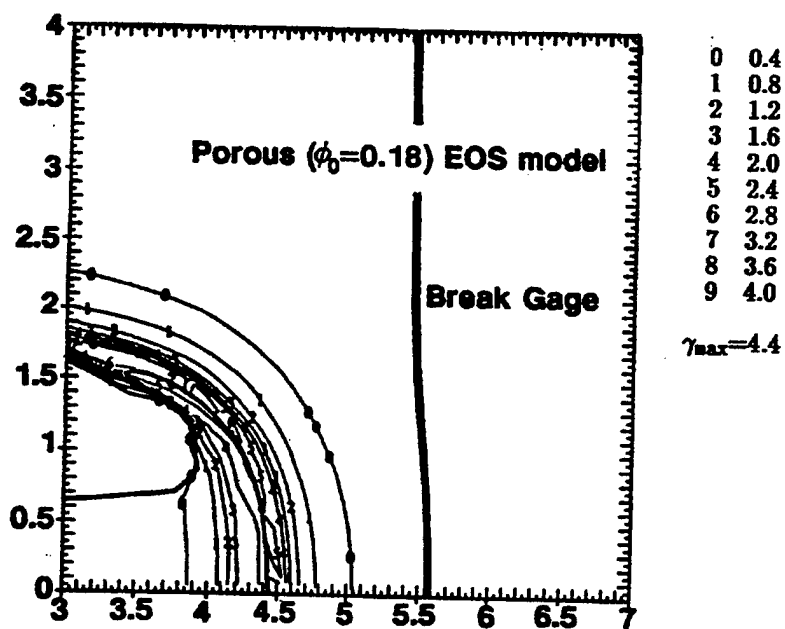
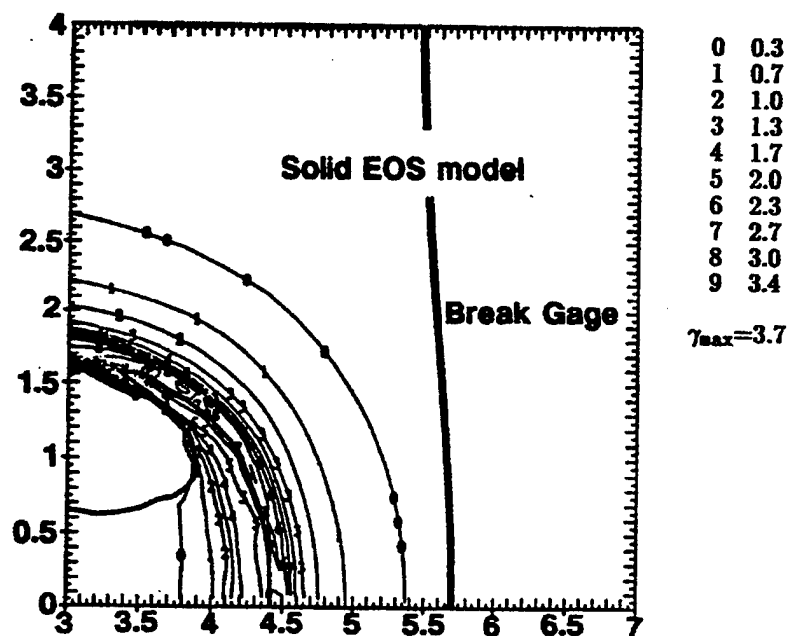
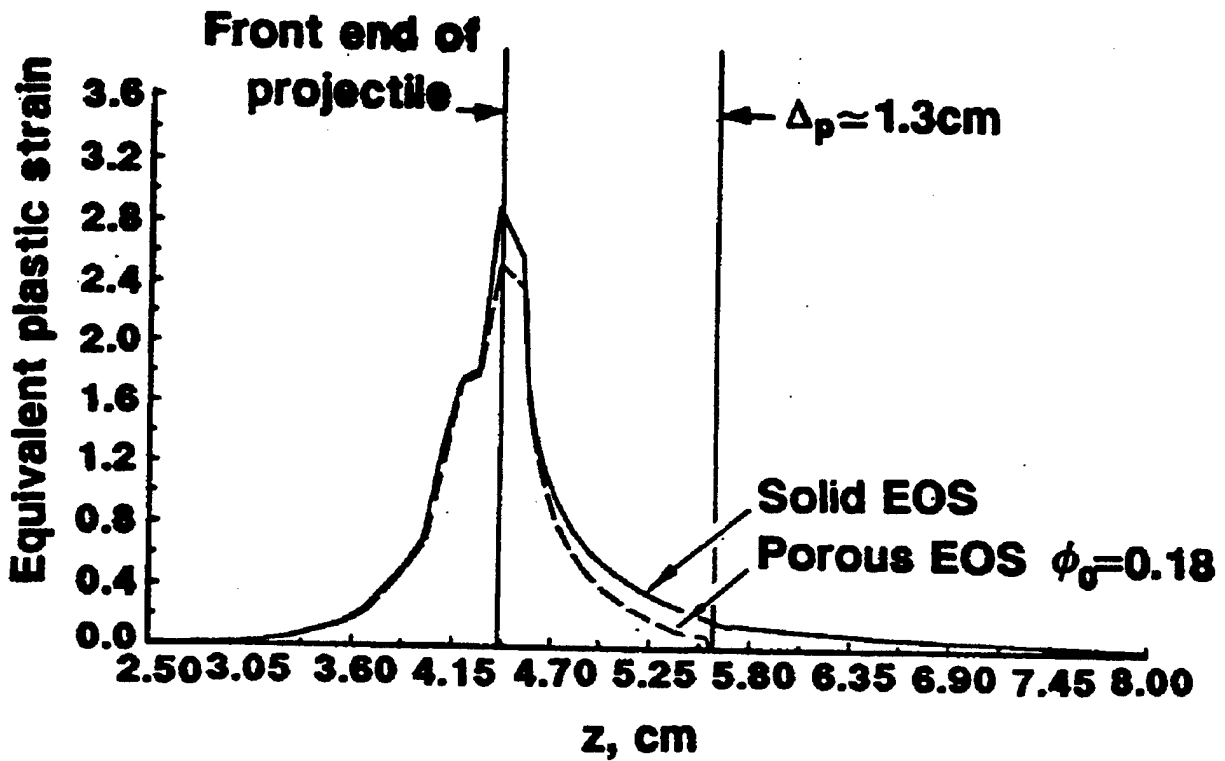


Figure 7
 Profiles of radial component of velocity v_r vs radial coordinate r calculated at $z = 5.0 \text{ cm}$ at time $t = 35 \mu\text{s}$



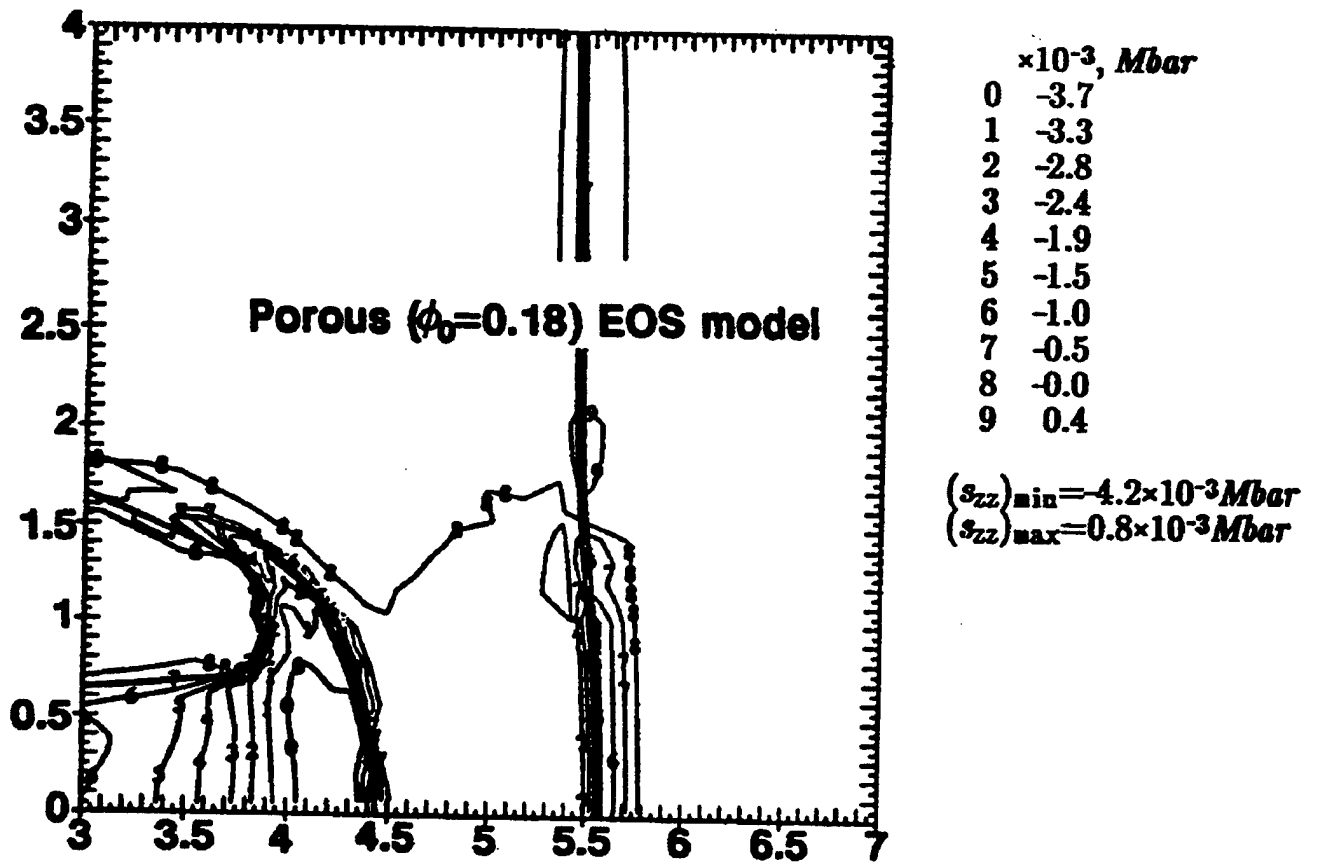
(Calculated at time $t = 35 \mu s$)

Figure 8
Effect of EOS model for concrete on configuration of flow field
in front of projectile - isolines of equivalent plastic stream



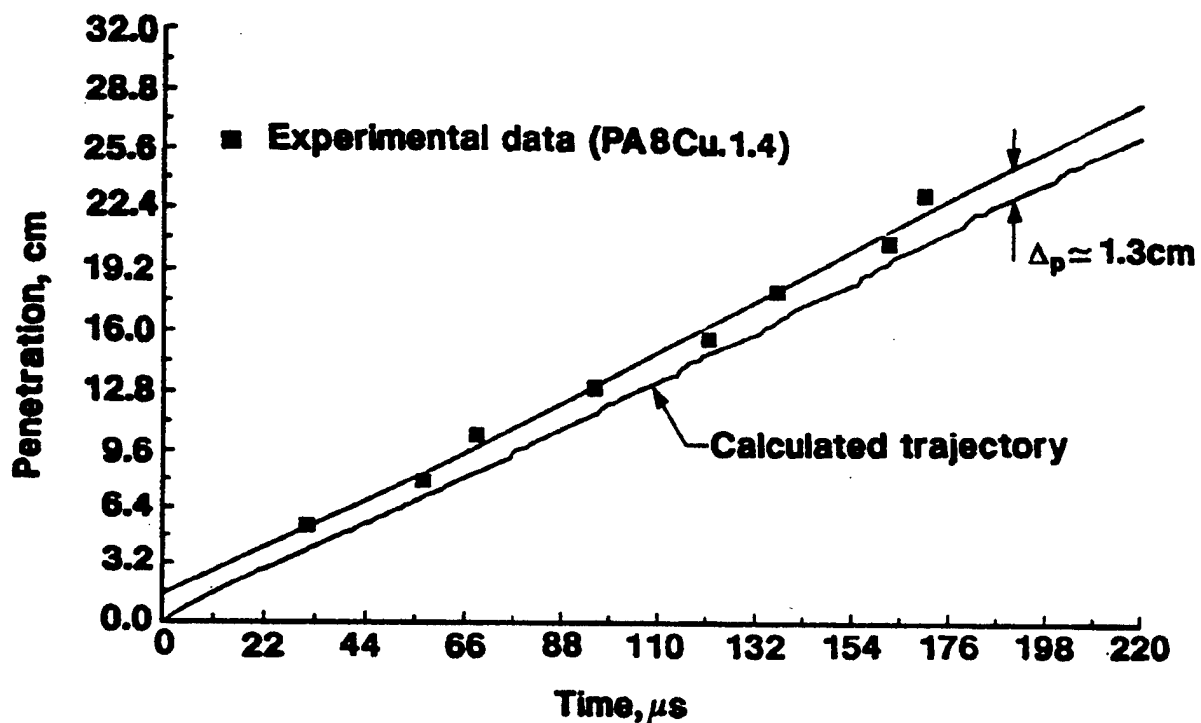
(Calculated at time $t = 35 \mu s$)

Figure 9
Effect of EOS model for concrete on configuration of flow field in front
of projectile - profiles of equivalent plastic strain vs
axial coordinate z for streamline $r = 0$



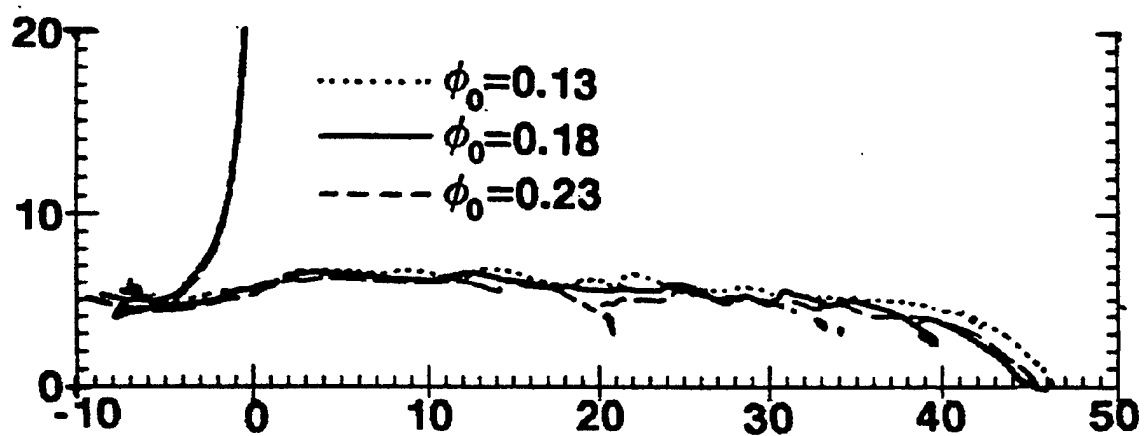
(Calculated at time $t = 35 \mu\text{s}$)

Figure 10
 Effect of EOS model for concrete on configuration of flow field in front
 of projectile - isolines of σ_{zz} component of stress deviator



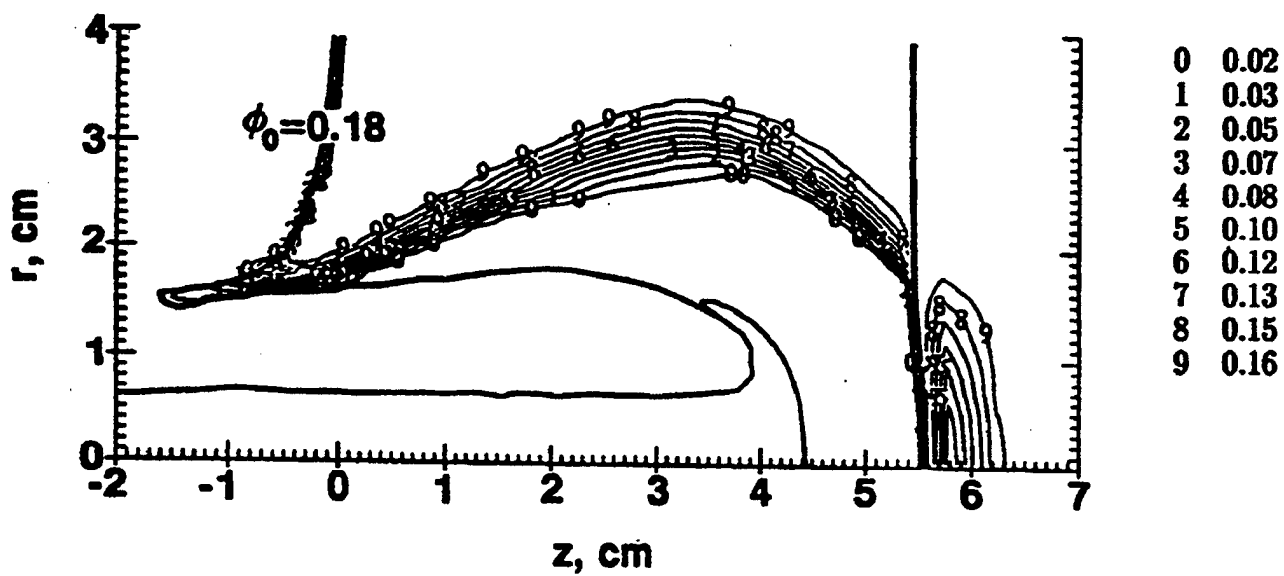
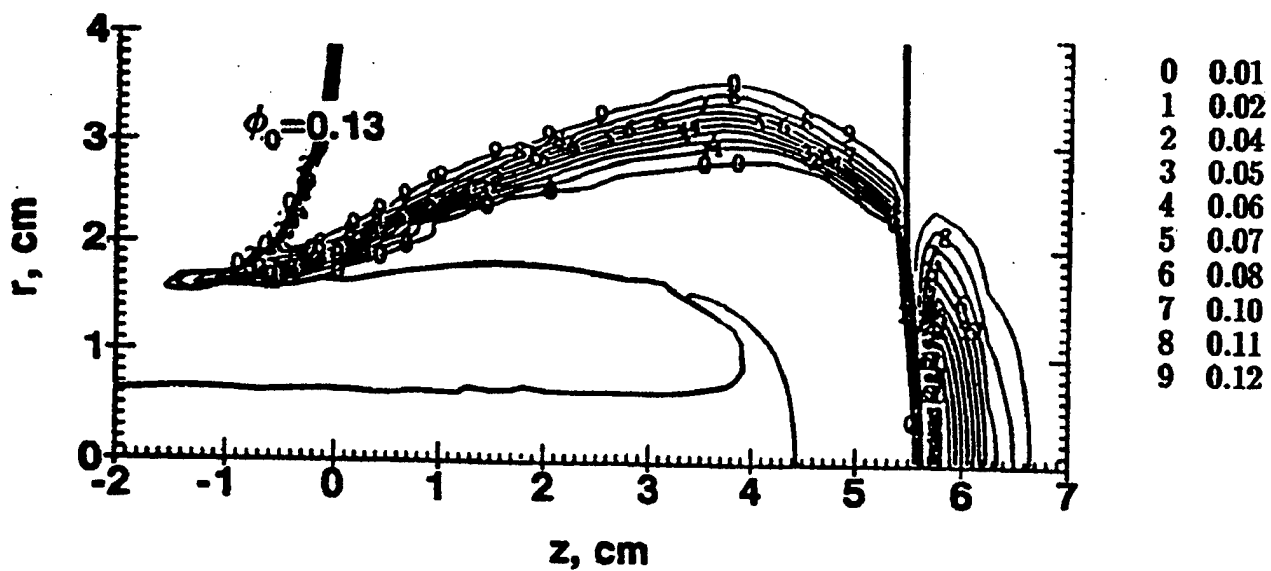
(The distance between the regression of trigger times and the trajectory of the front of the penetrator measures the size of the plastic flow field in the front of the projectile.)

Figure 11
Trajectory of front end of penetrator compared
with trigger times from break gages



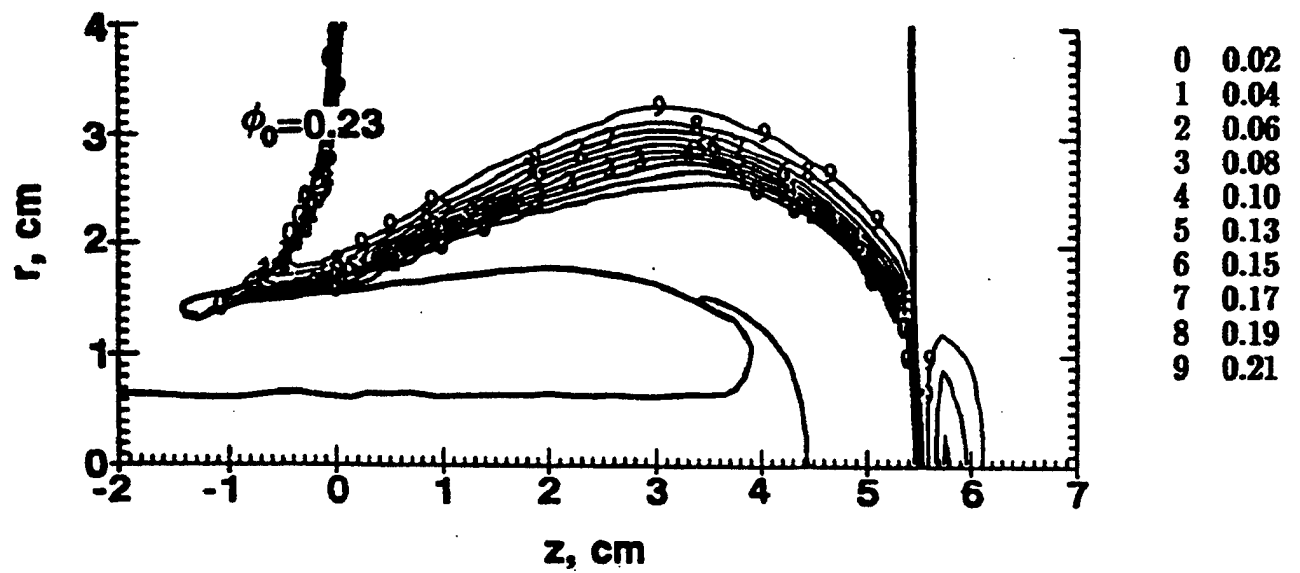
(Resulted in nearly identical penetration depths and hole profiles.)

Figure 12
Analysis with porous EOS model with values of initial porosity ϕ varying between 0.13 and 0.23



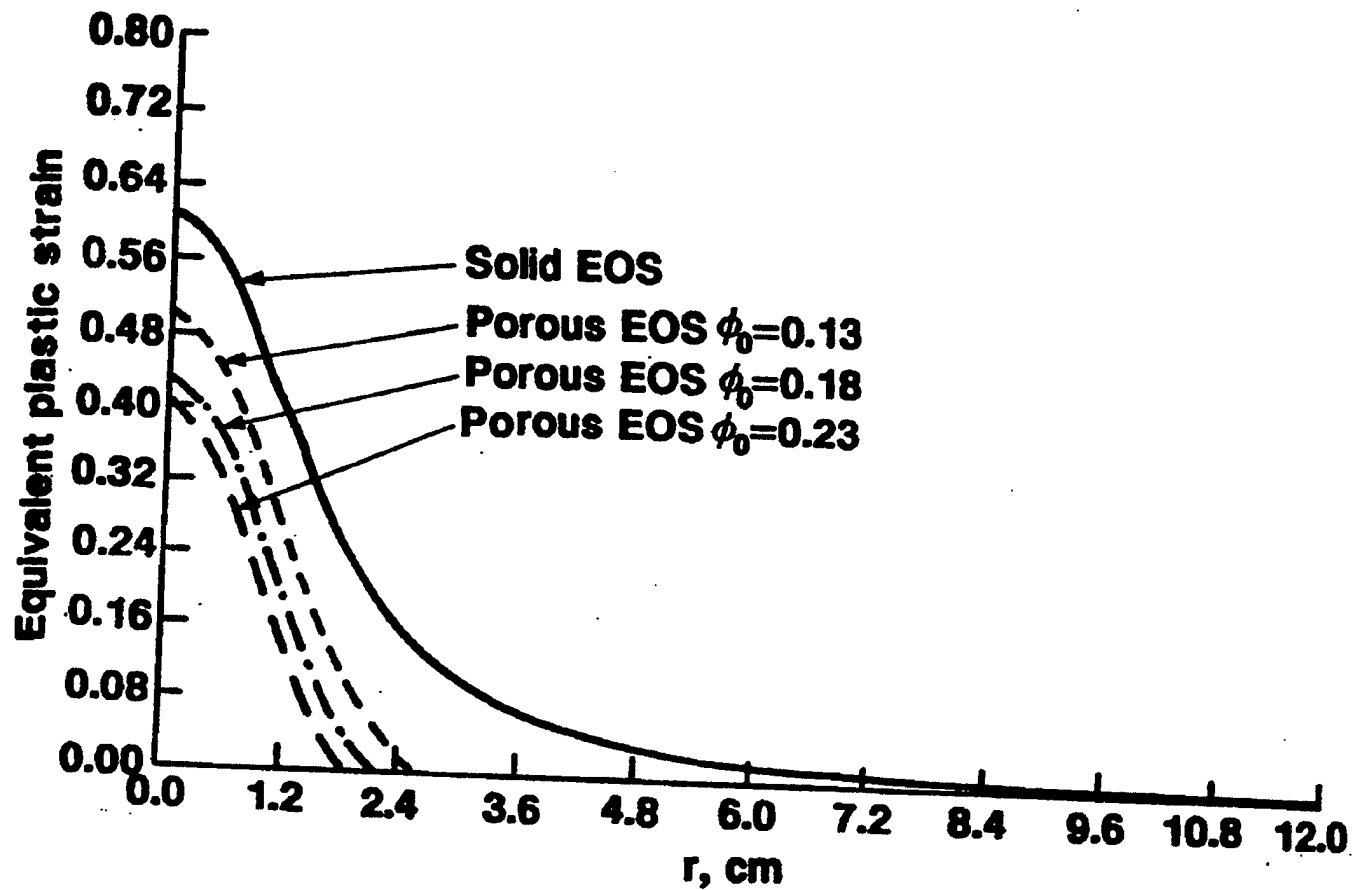
(Concrete adjacent to boundary of crater was crushed and all porosity was squeezed out.)

Figure 13
Isolines of porosity at time $t = 35 \mu s$ calculated with
different values of initial porosity (Part 1 of 2)



(Concrete adjacent to boundary of crater was crushed and all porosity was squeezed out.)

Figure 13
Isolines of porosity at time $t = 35 \mu s$ calculated with
different values of initial porosity (Part 2 of 2)



(Decreasing the value of initial porosity increases the size of plastic flow field in front of projectile.)

Figure 14
Equivalent plastic strain vs radial coordinate
 r at $z = 5.0$ cm at time $t = 35 \mu s$

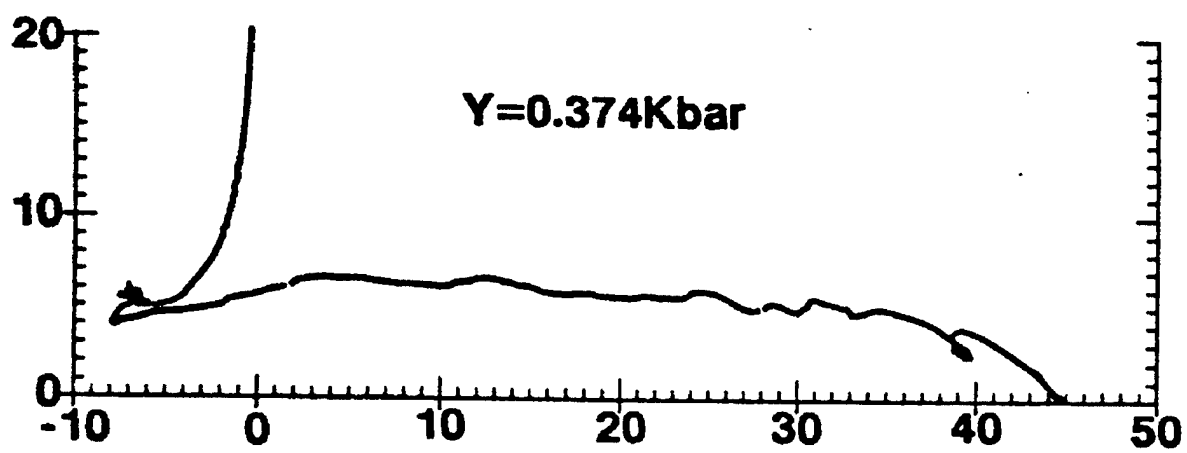
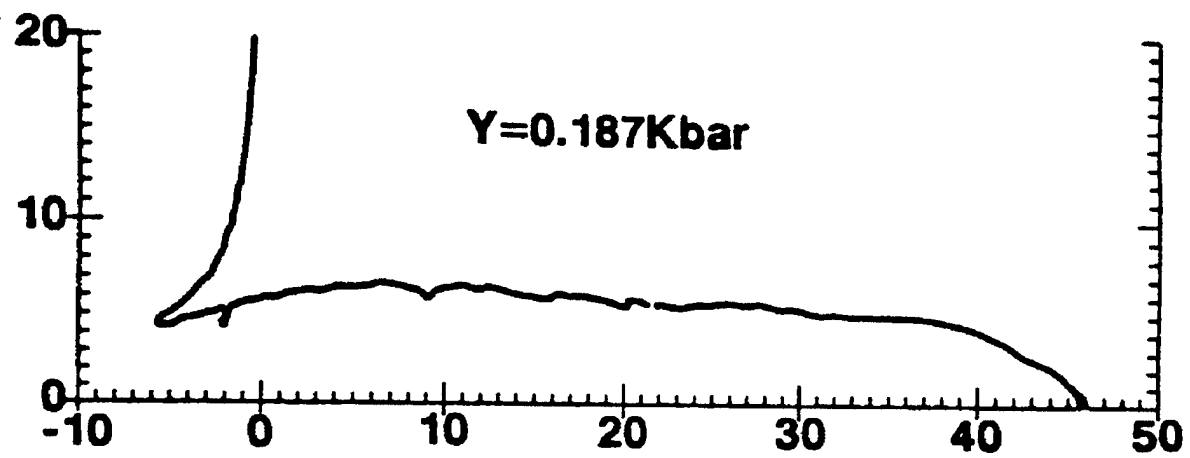


Figure 15
Hole profiles calculated with constant strength model for
varying values of von Mises strength Y (Part 1 of 2)

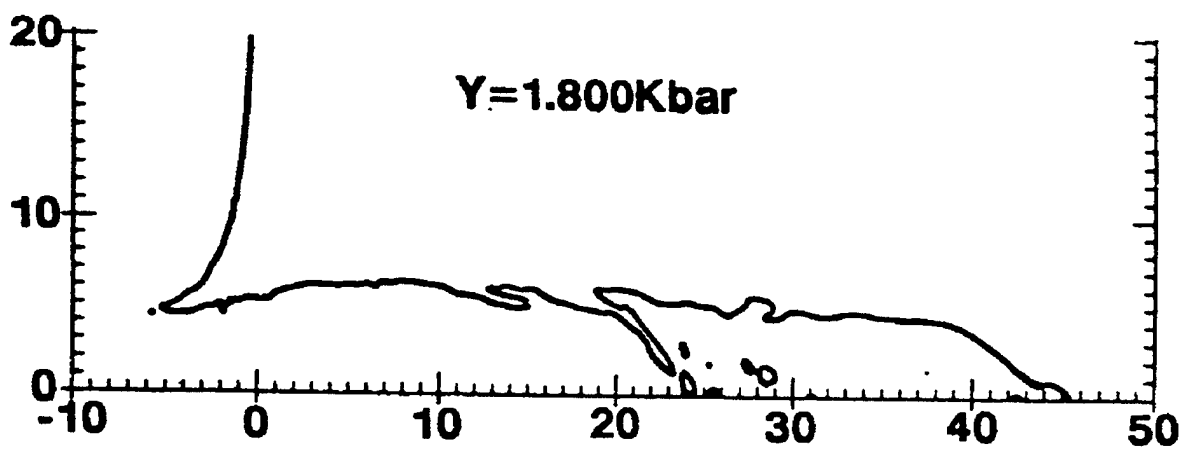
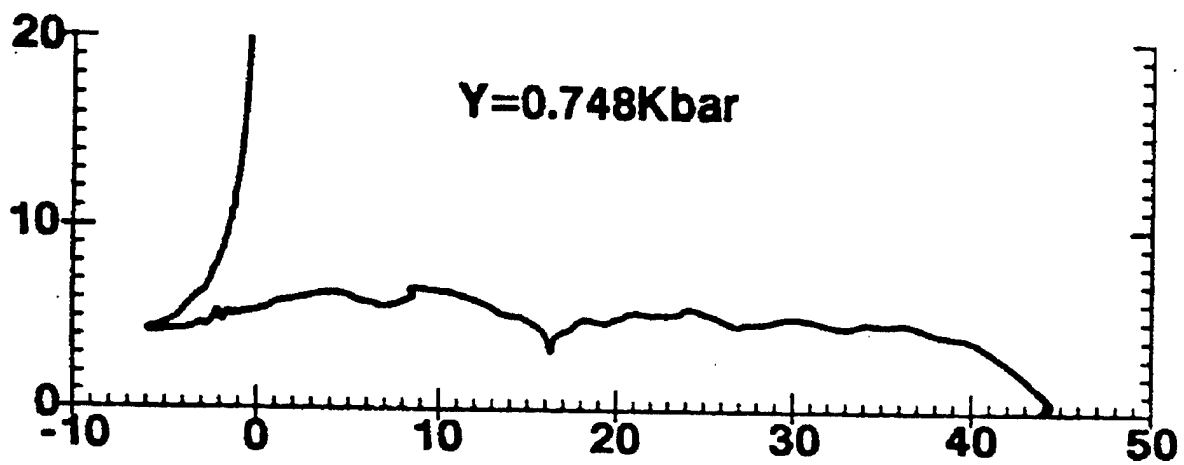


Figure 15
Hole profiles calculated with constant strength model for
varying values of von Mises strength Y (Part 2 of 2)

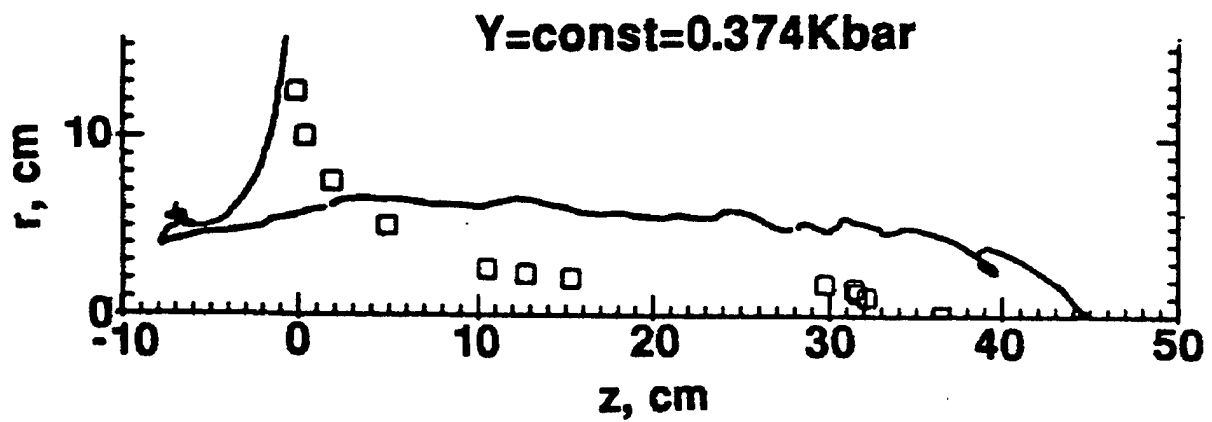


Figure 16
Hole profiles for constant strength models for concrete

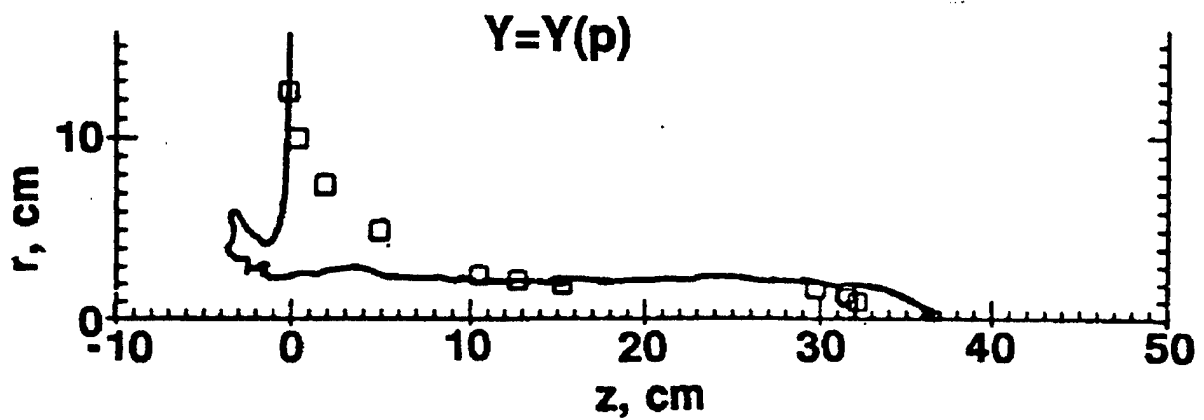


Figure 17
Hole profiles for pressure-dependent strength models for concrete

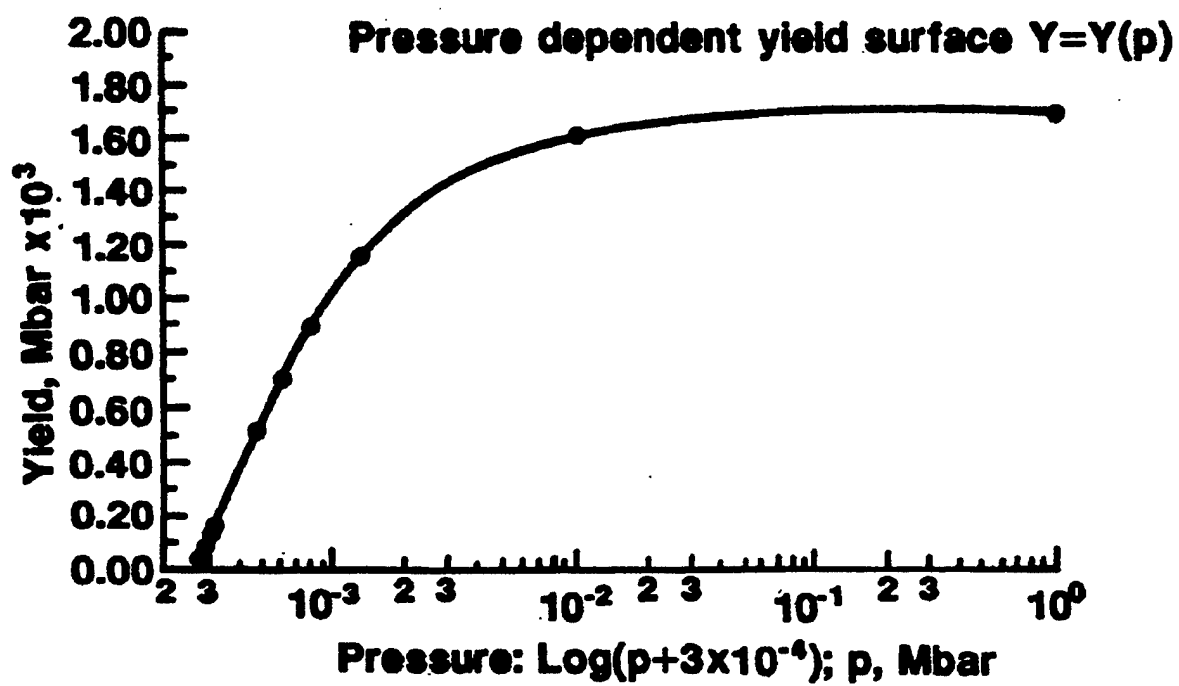
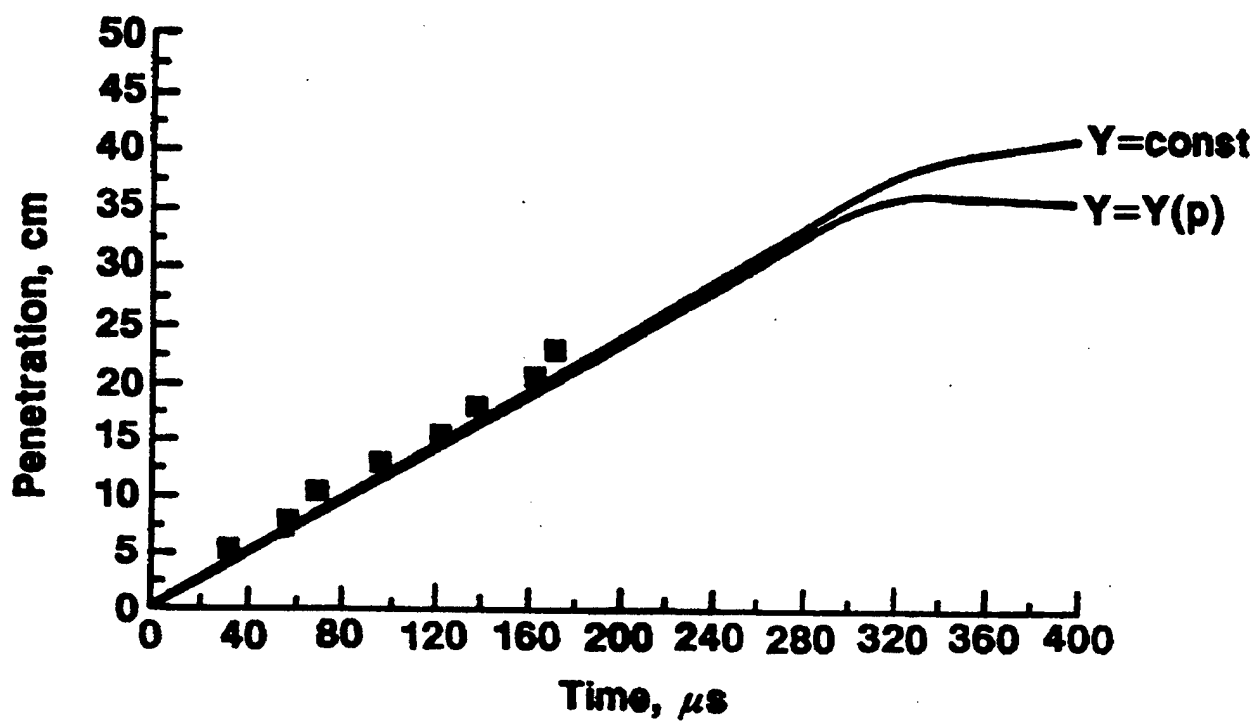


Figure 18
Pressure-dependent yield surface $Y = Y(p)$



(Calculated with constant strength and pressure-dependent strength models.)

Figure 19
Trajectory of front end of projectile

Table 1
Computations performance for 200 μ s of penetration time

File ID	Mesh Motion	Min/max sizes of computational cells, cm								No. of compt. cells	Required CPU time hr
		Zone 1		Zone 2		Zone 3		Zone 4			
		$\frac{\Delta z_{min}}{\Delta z_{max}}$	$\frac{\Delta r_{min}}{\Delta r_{max}}$	$\frac{\Delta z_{min}}{\Delta z_{max}}$	$\frac{\Delta r_{min}}{\Delta r_{max}}$	$\frac{\Delta z_{min}}{\Delta z_{max}}$	$\frac{\Delta r_{min}}{\Delta r_{max}}$	$\frac{\Delta z_{min}}{\Delta z_{max}}$	$\frac{\Delta r_{min}}{\Delta r_{max}}$		
pci0_00	Euler & ALE	0.0667 2.1670	0.0342 0.1920	0.0667 0.6670	0.0342 1.7520	0.2000 0.2540	0.0342 1.7520	9.2000 9.2000	0.0342 1.7520	29,895	102.2
pci0_01	Euler & ALE	0.0650 2.8250	0.0722 0.2000	0.1333 0.1333	0.0722 3.7190	0.1400 0.5080	0.0722 3.7190	0.1333 11.633	0.0722 3.7190	10,971	18.4
pci0_02	Euler & ALE	0.0650 2.8250	0.0722 0.2000	0.2500 0.2500	0.0722 3.7190	0.2330 0.5080	0.0722 3.7190	0.2333 11.633	0.0722 3.7190	9,437	9.4
pci0_02E	Euler	0.0650 2.8250	0.0722 0.2000	0.2500 0.2500	0.0722 3.7190	0.2330 0.5080	0.0722 3.7190	0.2333 11.633	0.0722 3.7190	9,437	30.4

(Benchmarked on a SUN 4/490 workstation for varying degrees of discretization and modes of grid motion.)

Table 2
Parameters for solid and porous EOS constitutive models

File ID	EOS Form	A_0	A_1	A_2	A_3	B_0	B_1	B_2	φ_0	ρ_0	ρ_r	Y_0	G	η_{min}
pccu_02_sol_f1	Solid	.0	.3122	.4396	.1693	.1	.1	.0	N/A	2.240	N/A	0.374	0.202	0.9934
pccu_02_por_f1	Porous	.0	.3122	.4396	.1693	.1	.1	.0	0.18	2.240	2.732	0.374	0.202	0.9962
pccu_02_por_f2	Porous	.0	.3122	.4396	.1693	.1	.1	.0	0.23	2.240	2.909	0.374	0.202	0.9962
pccu_02_por_f3	Porous	.0	.3122	.4396	.1693	.1	.1	.0	0.13	2.240	2.575	0.374	0.202	0.9962
pccu_03_Y_f2	Porous	.0	.3122	.4396	.1693	.1	.1	.0	0.18	2.240	2.732	0.187	0.202	0.9969
pccu_03_Y_f3	Porous	.0	.3122	.4396	.1693	.1	.1	.0	0.18	2.240	2.732	0.748	0.202	0.9969
pccu_03_Y_f4	Porous	.0	.3122	.4396	.1693	.1	.1	.0	0.18	2.240	2.732	1.496	0.202	0.9969
pccu_03_Y_f5	Porous	.0	.3122	.4396	.1693	.1	.1	.0	0.18	2.240	2.732	1.800	0.202	0.9969
pccu_03_YP_f1	Porous	.0	.3122	.4396	.1693	.1	.1	.0	0.18	2.240	2.732	$Y(p)$	0.202	0.9969

(A_i , B_{i-1} , $i = 1, 3$, and G are Mbar, Y_0 is in Kbar, ρ_0 and ρ_r are in g/cm^3 .)

REFERENCES

1. Schwer, L.E.; Rosinsky, R.; and Day, J., "An Axisymmetric Lagrangian Technique for Predicting Earth Penetration Including Penetrator Response," Int. J. Num. Anal. Metho. Geomech., Volume 12, pp. 235-262, 1988.
2. Heider, N., "3D-Finite Element Impact Simulation of Concrete Structures," Computational Technique for Contact, Impact, Penetration and Perforation of Solids, Schwer, L.E.; Salamon, N.J.; Liu, W.K. (eds.), AMSE AMD-Volume 103, pp. 359-372, 1989.
3. Adamik, V. and Matejovic, P., "A Contribution to Computational Modeling of Reinforced Concrete Structures Subjected to Impact Loading," Nuclear Engineering Design, Volume 113, pp. 111-120, 1989.
4. Bicanic, N. And Zienkiewicz, O.C., "Constitutive Model for Concrete Under Dynamic Loading," Earthquake Engineering Structure Dynamics, Volume 11, pp. 689-710, 1983.
5. Yarrington, P.; Silling, S.A.; Hertel, E.S., Jr.; and Rottler, J.S., "A Progress Report on the Runway Cratering Analysis Project," Sandia National Laboratories, Albuquerque, NM, 1991.
6. Tipton, R.E., "Porous EOS in CALE Used to Model Concrete," Lawrence Livermore National Laboratory, Livermore, CA, 1991.
7. Kerley, G.I., "CTH Equation of State Package: Porosity and Reactive Burn Models," Report no. SAND92-0553, Sandia National Laboratories, Albuquerque, NM, 1992.
8. Gold, V.M.; Pearson, J.C.; and Turci, J.P., "A Study of Impact Response of Concrete and Reinforced Concrete Targets for the Velocities *Circa* $0.2 \text{ cm}/\mu\text{s}$," Proceedings of the International Symposium of Impact Engineering, Volume 1, pp. 217-222, Sendai, Japan, 1992.
9. Weihrauch, G., "The Behavior of Copper Pins Impacting Different Materials at Speeds Between 50 m/s and 1650 m/s," ISL Report 7/71, Franco-German Research Institute, Saint Louis, France, 1971.
10. Lehr, H.F. and Weihrauch, G., "Target Deformations in Front of a Hydrodynamically Penetrating Rod Projectile, Analysis of Experiments," Technical Report RT 14/73, Franco-German Research Institute, Saint Louis, France, 1973.
11. Tipton, R.E., "CALE Users Manual," Version 910201, Lawrence Livermore National Laboratory, Livermore, CA, 1991.

REFERENCES

(cont)

12. Steinberg, D.J.; Cochran, S.G.; and Guina, M.W., "A Constitutive Model for Metals Applicable at a High-strain Rate," J. Appl. Phys., Volume 51, Number 3, pp. 1498-1504, 1980.
13. Tipton, R.E., "EOS Coefficients for the CALE Code for Some Materials," Lawrence Livermore National Laboratory, Livermore, CA 1991.
14. Gregson, V.G., Jr., "A Shock Wave Study of Fondu-Frye WA-1 and Concrete," General Motors Materials and Structures Laboratory Report MSL-70-30, General Motors Corporation, Warren, MI, 1971.
15. Read, H.E. and Maiden, C.J., "The Dynamic Behavior of Concrete," S-CUBED Report 3SR-707, Systems, Science and Software Corporation, La Jolla, CA, 1971.
16. Smith, J., Private Communications, Lawrence Livermore National Laboratory, Livermore, CA 1993.

DISTRIBUTION LIST

Commander
Armament Research, Development and Engineering Center
U.S. Army Tank-automotive and Armaments Command
ATTN: AMSTA-AR-LSL (2)
AMSTA-AR-GCL
AMSTA-AR-AEE
AMSTA-AR-AEE-W (3)

Administrator
Defense Technical Information Center (DTIC)
ATTN: DTIC-OCC (12)
8725 John J. Kingman Road, Suite 0944
Fort Belvoir, VA 22060-6218

Director
U.S. Army Material System Analysis Activity
ATTN: AMXSY-MP
Aberdeen Proving Ground, MD 21010-5423

Commander
Chemical/Biological Defense Agency
U.S. Army Armament, Munitions and Chemical Command
ATTN: AMSCB-CII, Library
Aberdeen Proving Ground, MD 21010-5423

Director
U.S. Army Edgewood Research, Development and Engineering Center
ATTN: SCBRD-RTB (Aerodynamics Technology Team)
Aberdeen Proving Ground, MD 21010-5423

Director
U.S. Army Research Laboratory
ATTN: AMRSL-OP-CI-B, Technical Library
Aberdeen Proving Ground, MD 21005-5066

Chief
Benet Weapons Laboratory, CCAC
Armament Research, Development and Engineering Center
U.S. Army Tank-automotive and Armaments Command
ATTN: AMSTA-AR-CCB-TL
Watervliet, NY 12189-5000

DISTRIBUTION LIST
(cont)

Director
U.S. Army TRADOC Analysis Command-WSMR
ATTN: ATRC-WSS-R
White Sands Missile Range, NM 88002

GIDEP Operations Center
P.O. Box 8000
Corona, CA 91718-8000